

# Antarctic sea ice types from active and passive microwave remote sensing

Christian Melsheimer<sup>1</sup>, Gunnar Spreen<sup>1</sup>, Yufang Ye<sup>2</sup>, and Mohammed Shokr<sup>3</sup>

<sup>1</sup>Institute of Environmental Physics (IUP), University of Bremen, Germany

<sup>2</sup>School of Geospatial Engineering and Science, Sun Yat-Sen University, Zhuhai, China

<sup>3</sup>Environment and Climate Change Canada, Toronto, Canada

**Correspondence:** Christian Melsheimer (melsheimer@uni-bremen.de)

Version 1.1.0, Wednesday 25<sup>th</sup> May, 2022, 13:39

## Abstract.

Polar sea ice is one of the Earth's climate components that has been significantly affected by the recent trend of global warming. While the sea ice area in the Arctic has been decreasing at a rate of about 4% per decade, the multi-year ice (MYI), also called perennial ice, is decreasing at a faster rate of 10%–15% per decade. On the other hand, the sea ice area in the Antarctic region was slowly increasing at a rate of about 1.5% per decade until 2014 and since then it has fluctuated without a clear trend. However, no data about ice type areas are available from that region, particularly of MYI. Due to differences in physical and crystalline structural properties of sea ice and snow between the two polar regions, it has become difficult to identify ice types in the Antarctic. Until recently, no method has existed to monitor the distribution and temporal development of Antarctic ice types, particularly MYI throughout the freezing season and on decadal time scales. In this study, we have adapted a method for retrieving Arctic sea ice types and partial concentrations using microwave satellite observations to fit the Antarctic sea ice conditions. The first circumpolar, long-term time series of Antarctic sea ice types; MYI, first-year ice and young ice is being established, so far covering years 2013–2021. Qualitative comparison with synthetic aperture radar data, with charts of the development stage of the sea ice, and with Antarctic polynya distribution data show that the retrieved ice types, in particular the MYI, are reasonable. Although there are still some shortcomings, the new retrieval for the first time allows insight into the evolution and dynamics of Antarctic sea ice types. The current time series can in principle be extended backwards to start in the year 2002 and can be continued with current and future sensors.

## 1 Introduction

As an important component of the global climate system, sea ice affects and reflects changes in other climate components, controls energy and gas fluxes between ocean and atmosphere in polar regions, and it is an important part of the polar marine ecosystem. The Arctic sea ice extent has decreased by 4.1% per decade in the past three decades (Parkinson and Cavalieri, 2012b), while the declining rate for multiyear ice (MYI), ice that has survived at least one summer melt (item 2.6, 2.6.x,

JCOMM Expert Team on Sea Ice, 2015), is much higher, 10–15% per decade (Johannessen et al., 1999; Comiso, 2012; Meredith et al., 2019). This ice, which is also called perennial ice, is the counterpart of seasonal ice which is defined as ice that forms in the beginning of the freezing season and melts in the following summer. Seasonal ice includes young ice (YI), which has thickness less than 30 cm (items 2.1–2.4 in JCOMM Expert Team on Sea Ice, 2015) and the more common first-year ice (FYI), which is thicker than 30 cm (items, 2.5.x in JCOMM Expert Team on Sea Ice, 2015). Three decades ago, MYI covered two thirds of the Arctic Basin. This portion has dropped to one third recently and the MYI has been replaced by FYI (Kwok, 2018).

In contrast to Arctic ice, sea ice extent in the Antarctic has increased by 1.5% per decade since the 1970s until 2014 (Parkinson and Cavalieri, 2012a). Since then, it has strongly decreased and than partly rebounded, so it is too early to quantify any new trend (cf. Ludescher et al., 2019; Parkinson, 2019; Parkinson and DiGirolamo, 2021). Only a small fraction of the sea ice in the Antarctic survives the summer and hence becomes MYI; it is mostly found in the Weddell Sea, but also on the Western side of the Antarctic Peninsula and in small patches around the coast (Stocker et al., 2013).

Almost all MYI in the Antarctic is in fact second-year ice (SYI) because it will usually have drifted out to lower latitudes and melt after at most 2 years. However, it is difficult to discriminate between SYI and older ice using satellite data directly (i.e., not using multi-annual satellite observation or drift data based on multi-temporal satellite imagery). For the remainder of this study, the term MYI usually denotes Antarctic second year ice. Unlike the Arctic, the evolution and spatial distribution of sea ice types in the Antarctic are still unclear. The MYI area of the Antarctic may have followed an increasing trend, based on the fact that in the Austral summer the sea ice extent of the Antarctic has increased by 3.6% per decade from 1979 to 2010 (Parkinson and Cavalieri, 2012a). As this is the sea ice which is becoming MYI, one might assume that the MYI area overall increased at a similar rate. In the absence of information on the sea ice type distribution and evolution, the ice mass balance and the energy fluxes between ocean and atmosphere are still unknown. MYI also is a good proxy for the total ice and snow thickness and thereby the MYI distribution influences energy fluxes and serves as an indicator or response to climate forcing.

In the Antarctic, sea ice cover, and particularly MYI, is different in many ways from Arctic ice. There is commonly a thicker snow cover, which may cause the underlying sea ice to be depressed below the water surface and thus be flooded, creating so-called flooded ice, and, when refreezing, snow ice. In addition, water from partial snow melt that percolates down and refreezes at the bottom of the snow layer forms so-called superimposed ice, which is more common in the Antarctic than in the Arctic (Haas et al., 2001). The ice cover in the Antarctic is also rougher than that in the Arctic because it is exposed to higher wind that triggers more motion and collisions between ice floes (Wadhams et al., 1986). The turbulent ocean water leads to formation of frazil ice crystalline structure, which is another difference compared to the mostly congealed structure of the Arctic sea ice (Gow et al., 1987; Lange and Eicken, 1991). For these reasons, statistical distributions of radiometric and backscattering observations are different between the two regions.

Most of the Antarctic MYI is found in the Weddell Sea. The Weddell Gyre transports the MYI away from the coast (where it has survived the summer), towards the north-western and northern Weddell Sea where eventually most of it melts. In turn, seasonal ice is transported into the Weddell Sea from the north and northeast, can be pressed and compacted against the ice shelves and the coast of the Antarctic peninsula where it survives the summer and becomes MYI. Spatial and temporal

observations of the MYI distribution are needed to better understand these processes. Beside MYI, the other ice types are of  
60 interest as well. Along the coasts large landfast ice areas develop regularly (Nihashi and Ohshima, 2015). Note that a substantial  
amount of the MYI along the East Antarctic coast is actually fast ice (Massom et al., 2010). This is often true MYI (older than  
two years) which is of great importance for the ecosystem and has effects on buttressing ice shelves. In polynyas, new and  
YI types alter the mass balance and surfaces fluxes. In the marginal ice zone (MIZ), pancake ice is a common occurrence;  
a substantial part of new ice is actually formed via pancake ice (Lange et al., 1989). Monitoring the dynamic and vast sea  
65 ice cover requires satellite observations. A physically consistent time series of sea ice types is needed to ascertain trends and  
quantify the interaction of sea ice within the climate system. Currently, climate models are not yet able to correctly reproduce  
realistic future scenarios of the Antarctic sea ice extent and especially regional patterns are not well reproduced (Mahlstein  
et al., 2013; Polvani and Smith, 2013; Hobbs et al., 2015; Turner et al., 2015; Zunz et al., 2013). In order to improve and  
better validate climate models, time series with more detailed information about the sea ice, e.g., sea ice thickness or type, are  
70 required. Models usually do not directly produce our sea ice types as output variable, but rather sea ice age – which might well  
be set into relation with sea ice types like FYI and MYI.

The concentration of total sea ice and of the sea ice types (i.e., the area fraction of ice, in per cent, within an observation  
cell) can be estimated from microwave satellite observations because in this spectral range different ice types have different  
emission and scattering properties. This has long ago already been used by sea ice concentration retrieval algorithms using  
75 passive microwave (i.e., radiometer) data, like the NASA TEAM algorithm which retrieves FYI and MYI concentration. This,  
however, has been applied almost exclusively to the Arctic. Besides, the retrieved Arctic MYI tends to increase during the cold  
season which is not possible (see Section 3.2). Sea ice type discrimination based on analysing high-resolution active microwave  
(i.e., synthetic aperture radar) data usually lacks full and daily coverage. Using radar scatterometer data might give full and  
frequent coverage, but has ambiguities. There are very few attempts to retrieve sea ice types in the Antarctic, notably by Lythe  
80 et al. (1999) and Ozsoy-Cicek et al. (2011), but they are both only of regional scope.

Recently, a method has been developed to estimate partial and total concentration of Arctic ice types using a combination of  
active and passive microwave satellite measurements (i.e., from scatterometer and radiometer, respectively) and additional an-  
cillary data of air temperature and ice drift vectors. The method is based on Environment Canada's Ice Concentration Extractor  
algorithm, ECICE (Shokr et al., 2008; Shokr and Agnew, 2013) and subsequent correction schemes for mitigating misclassi-  
85 fications caused by melt-refreeze cycles and by snow metamorphosis. These correction schemes use surface temperature from  
meteorological reanalysis and ice drift from satellite data. This has been successfully applied and tested in the Arctic (Ye et al.,  
2016a, b) and has recently also been compared to other sea ice type retrieval results (Ye et al., 2019). In this study, we show  
that this method (i.e., ECICE and the correction schemes) can be adapted to Antarctic conditions. The study is first intended  
as a "proof of concept", but the ultimate goal is of course to eventually fill the data gap in the Antarctic – the lack of ice type,  
90 in particular, multiyear ice, data. The only other approach of operationally retrieving sea ice type in the entire Antarctic from  
remote sensing data is the ice type classification based on microwave radiometer data, recently (summer 2021) released by the  
Ocean and Sea Ice Satellite Application Facility (OSI-SAF) (Aaboe et al., 2021a).

This paper is organised as follows: In Section 2 we give a brief account of ECICE, the implemented correction schemes, and the adaptation to the Antarctic conditions. In Section 3, results of the Antarctic sea ice type concentration mapping are compared with data from other sources like Sentinel-1 radar images or ice charts, followed by critical discussion of the findings and the first time series of Antarctic MYI, 2013–2021. In Section 4 presents a summary and conclusions.

## 2 Estimation of Sea Ice Type Concentration

Satellite-based estimation of the total ice concentration and of partial concentration of different ice types like MYI, FYI and YI can be obtained using the Environment Canada’s Ice Concentration Extractor (ECICE). It takes input from any set of satellite observations and produces concentrations of any given ice types (Shokr et al., 2008). Our estimation of MYI concentration actually is a two-step procedure that first uses ECICE and then applies two correction schemes to the output MYI concentration in order to account for anomalies of the ECICE results (Ye et al., 2016a, b). One anomaly causes misclassification of MYI as FYI (usually observed in autumn) and the other causes misclassification of FYI as MYI (usually observed in spring).

### 2.1 ECICE – Environment Canada’s Ice Concentration Extractor

ECICE can take passive and active microwave satellite measurements as input. Possible passive microwave input data are from the satellite microwave radiometers Special Sensor Microwave/Imager (SSM/I, 1987-2009), Special Sensor Microwave/Sounder and Imager (SSMIS, 2003-2022), Advanced Microwave Scanning Radiometer for EOS (AMSR-E, 2002-2011) and Advanced Microwave Scanning Radiometer 2 (AMSR2, 2012-present). As AMSR-E and AMSR2 have considerably higher spatial resolution than SSM/I and SSMIS, we have used only their data so far. The measured quantities are the brightness temperatures at different frequencies and at vertical (V) as well as horizontal (H) polarisation. Possible active microwave input data include scatterometer measurements from QuikSCAT (1999-2009) and Advanced Scatterometer (ASCAT, 2007-present). The measured quantity is the backscattering coefficient (normalised radar backscattering cross section) at one or two polarisations (HH and VV). The number of input parameters to ECICE must be equal or greater than the number of the surface types to be distinguished. Here we use four surface types; namely open water, young ice (YI), first-year ice (FYI), and multiyear ice (MYI). The input parameters are listed in Table 1 and explained in Section 2.3.

Most methods that retrieve the concentration of sea ice or sea ice types from radiometer or radar data use representative values of each input parameter for each surface type (ice or ice types, open water) – these representative values are known as tie points (see, e.g., the 11 sea ice concentration algorithms compared by Ivanova et al. (2015): All but one (ECICE) use tie points, including all “standard” ones like NASA Team or Bootstrap algorithms). In contrast, ECICE uses the statistical distribution of all possible values of each input parameter for each surface type. Such distributions are obtained by sampling data of the given input parameter from the given surface obtained under different meteorological, dynamic and freezing conditions. The distributions have been established for the application of Arctic sea ice (Shokr et al., 2008; Ye et al., 2016a) and re-established here for the Antarctic application (see details in Section 2.3). Note, however, that under permanent melting conditions in



summer, the radiometric and backscattering properties of sea ice change drastically and the differences between the ice types  
125 diminish or even vanish. Therefore, sea ice type retrieval with ECICE is not possible in the melt season.

With the input parameter distributions for the different surface types, which can be interpreted as probability densities, a  
number  $n$  of possible realisations of tie points for all surfaces is selected using a random number generator. Here, we use  
1000 realisations. For any given observation in remote sensing data, the observation is considered to represent a linear mixture  
of typical values (tie points) for each surface type, weighted by the area fraction of that surface type in the observation cell.  
130 Therefore, a set of linear equations (equal to the number of observations) in which each equation represents decompositions  
of each input observation into its components from the given surface types is then constructed. The equations are solved  
simultaneously for the area fraction of each surface type under the constraint that all fractions must add up to one (equality  
constraint) and that each area fraction must be between 0 and 1 (inequality constraint). This formulates the problem into  
an inequality constrained optimisation problem, which is solved to find the ice concentrations that minimise a given cost  
135 function. Then, the median of the  $n$  solutions for the area fractions (i.e., concentrations) is produced from which the final  
answer is generated: a set of concentrations of the given ice types, each of them between 0% and 100%, adding up to the  
total ice concentration, and always adding up to 100% when the open water fraction is included. In addition to the ice type  
concentrations, the spread of the  $n$  solutions around the median is used as a measure of confidence of the result for each surface  
type (see details in Shokr et al., 2008), and is saved along with the output. To summarise briefly: First we calculate, for each  
140 surface type, the mean absolute deviation,  $MAD$ , of the  $n$  solutions from the median. Then the confidence level is

$$CL = 1 - \frac{MAD}{AD_{max}} \quad (1)$$

where  $AD_{max}$  is the maximum absolute deviation of the  $n$  results from the median. The confidence level is between 0.0  
(meaning: almost all results have large deviation from the median) and 1.0 (meaning: all results are identical).

## 2.2 Correction schemes

145 The determination of the ice type concentrations (i.e., the area fractions of the three ice types) is only based on their radiometric  
and backscattering properties. During atmospheric warm spells, commonly occurring in the transition seasons, snow wetness  
develops. The return of cold temperatures may cause snow metamorphism, and even without warm spells, snow metamorphism  
can occur over time. Both effects, snow wetness and snow metamorphism, cause anomalous microwave observations that make  
MYI appear as FYI and vice versa. Another process that causes anomalous observations is ice surface deformation at floe edges  
150 (e.g., pancake ice), which makes brightness temperature and backscattering from FYI look similar to those from MYI. Such  
errors are reduced by the two corrections schemes described in the following sections.

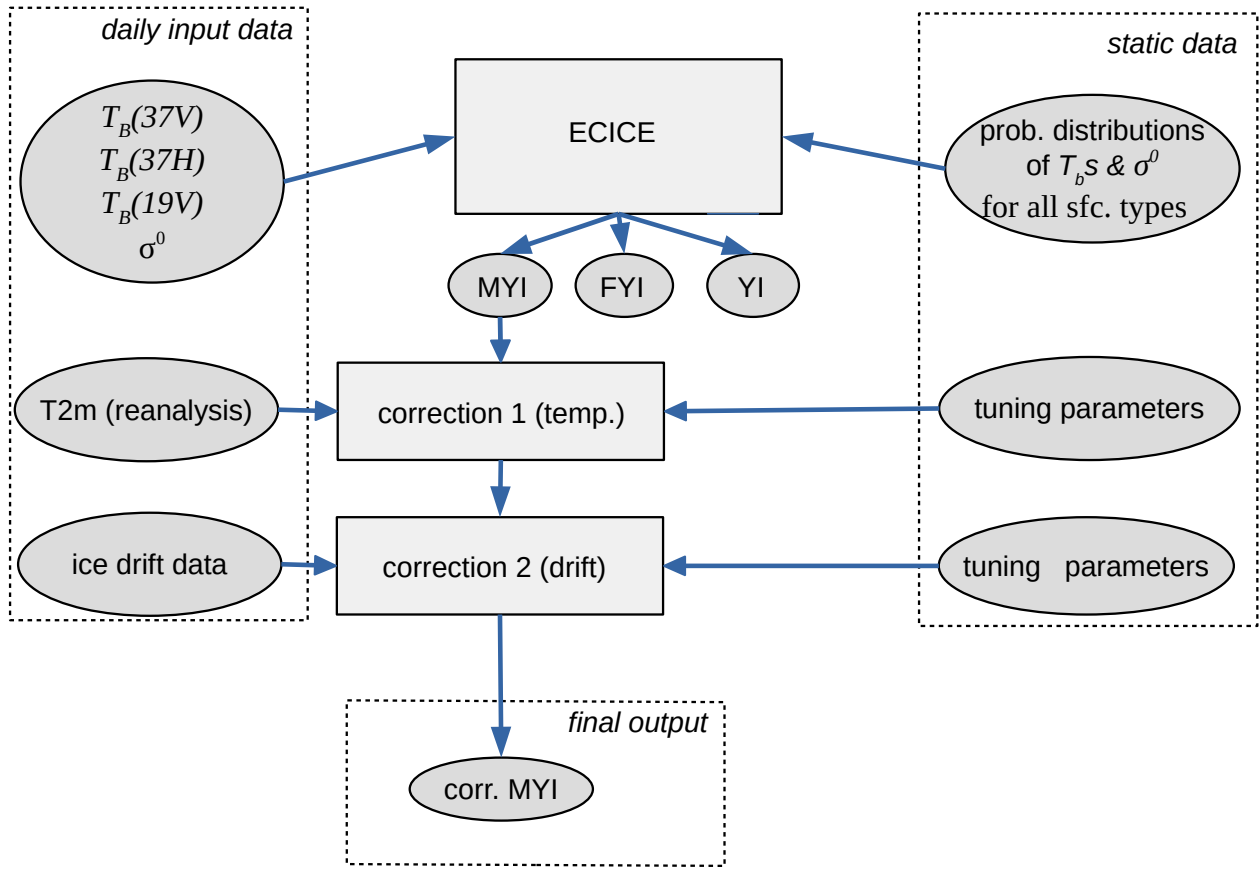
### 2.2.1 Temperature Correction

Warm air advection can occur during fall and spring seasons. When air temperature rises to near melting or beyond melting  
conditions, snow wetness develops and MYI will have lower backscatter and higher brightness temperature, typical of FYI.  
155 Therefore, it is misclassified by ECICE as FYI (more precisely: the retrieved MYI concentration is too low and the FYI con-

centration too high). After the end of the warm event, which typically takes between one to a few days, the correct classification is resumed. In order to account for this error, the so-called temperature correction scheme (Ye et al., 2016a) examines the 2-m air temperature ( $T_{2m}$ ) data to identify warm episodes of up to  $N$  days. Each episode starts with temperatures rising above a threshold  $T_1$  (near freezing temperature) and ends with temperatures falling below a threshold  $T_2$ . If the MYI concentration drops at any location affected by the warm spell by more than a specified threshold  $\Delta C_t$  and later rises again, such MYI concentrations are replaced by values linearly interpolated from before and after the warm episode. The values of the “tuning” parameters  $N$ ,  $T_1$ ,  $T_2$  and  $\Delta C_t$  used here are explained and specified in Section 2.3 (Table 2).

### 2.2.2 Drift Correction

Since the warm temperatures in the spring may progress for the rest of the season, the above temperature correction may not hold because it depends on the returning to the normal cold winter temperatures. For this reason, another correction was developed to identify locations of estimated MYI which are not realistic. This correction is based on the fact that MYI starts by definition as all remaining ice at the end of the melting season, i.e., at the onset of freeze-up. After that, during the cold season, no new MYI can be generated. MYI can then only drift, and its concentration can only be changed by divergence, convergence, and melting. Therefore, MYI is unrealistic if it appears at locations to which it cannot have drifted. To identify such locations, daily ice drift data are used to implement what is called “drift correction” (Ye et al., 2016b). This correction starts with defining the boundary of MYI cover from the map of a given day, using a threshold of 20% MYI concentration. The boundary is then adjusted according to the ice drift map of the same day to predict its contour in the next day. This is done by applying ice motion vectors (obtained from the sources mentioned below) to all pixels inside the boundary. This domain is then further extended by one grid cell to the outside in order to account for uncertainty of the ice drift product. Any MYI that has been retrieved outside of this domain cannot be multiyear ice but is FYI or YI that has radiometric and scattering properties that resemble MYI because of deformation or snow metamorphosis or other “ageing” processes of the ice. Therefore, all non-zero MYI concentrations in grid cells outside the mentioned domain are set to zero. However, this spurious MYI is in fact FYI or YI that has anomalous radiometric and scattering properties (so that ECICE has classified it as MYI), but there is no way of telling which of the two (YI or FYI) it actually is. Therefore, we keep as a new pseudo-ice-type which we call non-MYI. In addition, this correction scheme includes correction for some effects of snow metamorphosis for pixels inside the MYI contour of the given day which would make FYI radiometrically similar to MYI. It looks for sudden (within one day) rises,  $\Delta C_d$ , of MYI concentration concurrent with sudden reductions,  $\Delta T_{37}$ , of  $T_{B,37V}$  (brightness temperature at 37 GHz, vertical polarisation) or reductions,  $\Delta T_{19-37}$ , of  $T_{B,19H} - T_{B,37H}$  (difference of the brightness temperatures at 19 GHz and 37 GHz, horizontal polarisation). The latter difference is also called horizontal range, HR, and is used by Drobot and Anderson (2001) to identify the onset of snow melt. The use of this parameter in the drift correction is explained in detail in Ye et al. (2016b). In cases of such anomalies, the MYI concentration at the given pixel is replaced by the value of the previous day. The values of the “tuning” parameters  $\Delta C_d$ ,  $\Delta T_{37}$ , and  $\Delta T_{19-37}$  used here are explained and specified in Section 2.3 (Table 3). A final note on the name of this correction scheme: we call it drift correction here because it uses sea ice drift data to correct for the effect of



**Figure 1.** Flowchart of ECICE and the two correction schemes as well as the different types of input data. Note: prob. = probability; sfc. = surface

snow metamorphism and ice deformation and other processes that make YI and FYI resemble MYI for the ECICE retrieval. It does not correct for drift effects.

A flow chart showing ECICE, the two correction schemes and the various types of input data is shown in Figure 1

### 2.3 Adapting ECICE algorithm to the Antarctic sea ice

In order to use ECICE and the correction schemes for the Antarctic, the algorithms themselves do not need to be adapted. Instead, for ECICE, we need input parameter distributions derived from Antarctic data because Antarctic sea ice is different from Arctic sea ice (see Section 1). For the correction schemes, we might need to adapt the tuning parameters. The Antarctic implementation of ECICE at the IUP, University of Bremen, uses as input microwave radiometer data of the sensors AMSR-E (Advanced Microwave Scanning Radiometer for EOS) on the NASA satellite Aqua (2002–2011), or AMSR2 (Advanced

**Table 1.** Input parameters (“channels”) used in Antarctic sea ice type retrieval with ECICE. Note:  $T_B$  is brightness temperature,  $GR$  is gradient ratio (see Equation (2)),  $\sigma^\circ$  is normalised radar backscattering cross section.

Instrument	Parameter	Frequ. [GHz]	Polarisation
AMSR2	$T_B$	37	V
AMSR2	$T_B$	37	H
AMSR2	$GR$	19, 37	V
ASCAT	$\sigma^\circ$	5.3	VV

Microwave Scanning Radiometer 2) on the JAXA satellite GCOM-W1 (since 2012), and scatterometer data from ASCAT (Advanced Scatterometer) on the European polar-orbiting satellites MetOp-A, MetOp-B, and MetOp-C. The input parameters  
 200 (“channels”) we use are the same as for the Arctic sea ice type retrieval (Ye et al., 2016a, b), they are listed in Table 1. The gradient ratio at 19 and 37 GHz, V polarisation is defined as

$$GR(37V, 19V) = \frac{T_{B,37V} - T_{B,19V}}{T_{B,37V} + T_{B,19V}} \quad (2)$$

For all input parameters, we use daily gridded data, projected on a polar stereographic grid with a nominal resolution of 12.5 km. This is the common grid used by the National Snow and Ice Data Center, NSIDC (see more details in Melsheimer  
 205 and Spreen, 2019). The grid spacing is close to the resolution and the sampling interval of the original swath data of the used AMSR2 channels, which is 10 km (note that the footprint size is 7 km by 12 km at 36 GHz and 14 km by 22 km at 19 GHz). For the gridding, we combine all swaths of one day and then interpolate to the target grid (NSIDC polar stereographic) using a distance-weighted near-neighbour approach with four sectors, from the Generic Mapping Tools (GMT, Wessel et al., 2013). Before the gridding, the ASCAT data (normalised radar backscatter cross section,  $\sigma^\circ$ ) are converted to a common incidence  
 210 angle of  $40^\circ$ , using a simple linear approach for the dependence of  $\sigma^\circ$  on the incidence angle, based on a regression analysis of  $\sigma^\circ$  values over sea ice.

In order to derive the probability distributions of the input parameters needed by ECICE, we have to find appropriate sampling areas for three ice types, i.e., MYI, first-year ice (FYI), and young ice (YI). The sample areas from which the distributions were derived were chosen as follows: For FYI and MYI, we used the time evolution of total sea ice from the operational ASI  
 215 sea ice concentration retrieval in the year 2018<sup>1</sup>: At the beginning of the cold season, all remaining ice (mainly in the Weddell Sea) is MYI by definition. <sup>2</sup> Later in the season, sea ice that has formed in the season “away” from the MYI is FYI – taking into account, of course, that MYI can drift 10 km per day. For reliable samples of YI, we have used a satellite-based polynya data set from 2018 which is based on the Polynya Signature Simulation Method (PSSM, Markus and Burns, 1995) in the implementation by Kern et al. (2007), using combinations of the 36 GHz and 91 GHz, H and V polarisation channels  
 220 of the Special Sensor Microwave Imager/Sounder (SSMIS). We use the NRT data provided by ICDC/CEN, University of

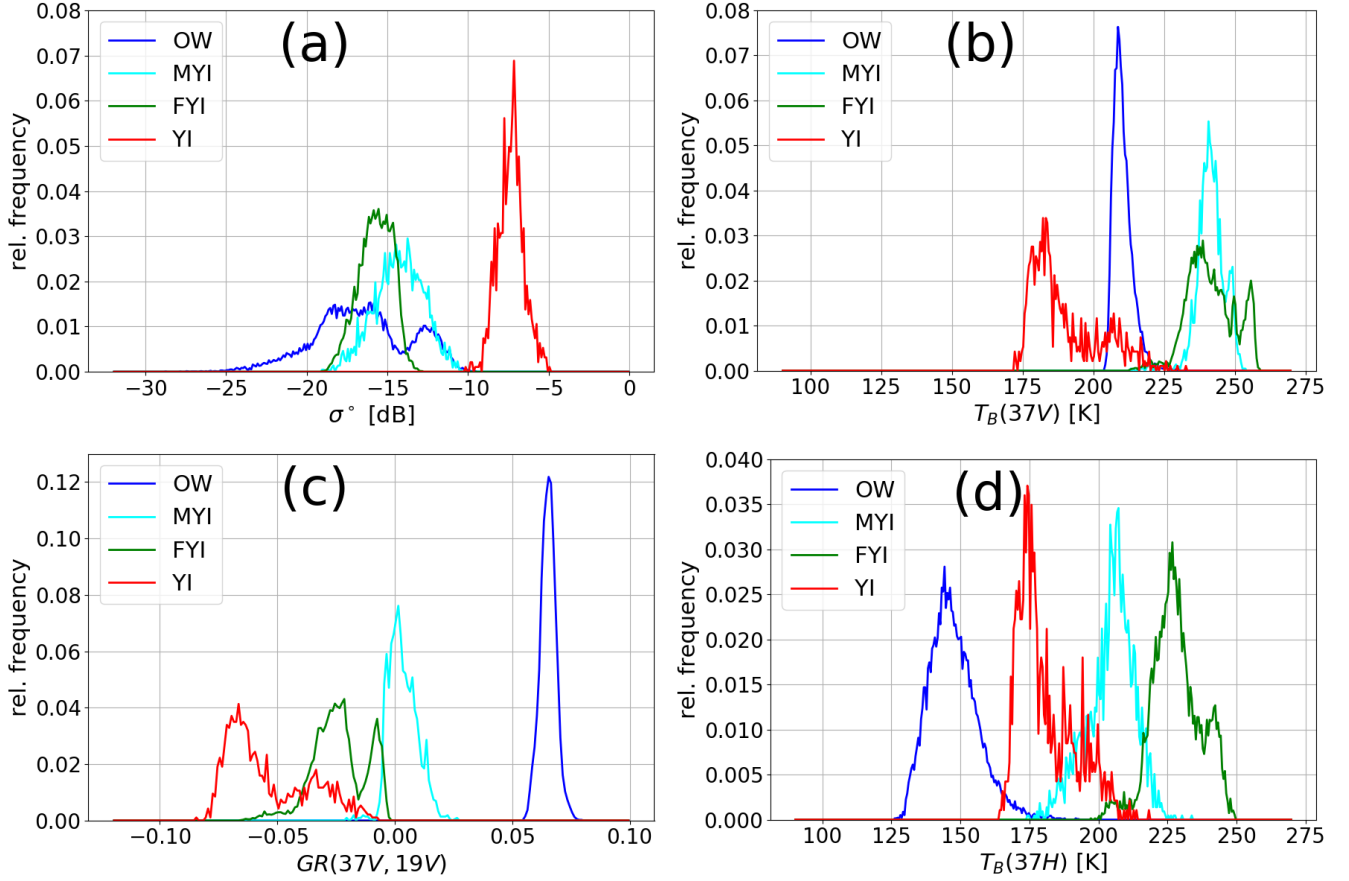
<sup>1</sup> ARTIST Sea Ice (ASI) algorithm (Spreen et al., 2008) <https://seaice.uni-bremen.de/sea-ice-concentration/>, Melsheimer and Spreen (2019)

<sup>2</sup>For this purpose, we define the beginning of the cold season directly from the daily ASI sea ice concentration maps as the day when the sea ice concentration and extent starts to grow again, regionally.

Hamburg (see details at <https://www.cen.uni-hamburg.de/en/icdc/data/cryosphere/polynya-antarctic.html>), region “Western Ross Sea”. The data contain a surface class “thin ice”, up to 20 cm thick, which was used here for YI (note, however, that it could be thicker ice but lower ice concentration). For the surface type “open water”, sample areas in the Southern Ocean in August 2018 and in the ice-free part of the Ross Sea in March 2018 were taken. Details of all the sample areas are listed in Appendix A. The resulting distribution functions of the four input parameters for the surface types YI, FYI, MYI and open water are shown in Figure 2. It is obvious that the four surface types cannot be distinguished using a single input channel, as the distributions generally overlap. However in some channels one specific surface type has a peak separated from the others, e.g., the backscatter ( $\sigma^\circ$ ) of MYI (Figure 2(a), red curve), or  $GR(37V,19V)$  of OW (panel (c), blue curve). In addition, there are pairs of mutually non-overlapping distributions, such as OW and YI for  $T_B(37V)$  (panel (b), blue and cyan curves), or OW and FYI for  $T_B(37H)$  (panel (d), blue and green curves). Comparing the distributions for brightness temperatures at 37 GHz, V and H polarisation ( $T_B(37V)$  and  $T_B(37H)$ , respectively) to corresponding Southern Hemisphere tie points for the NASA Team and the Bristol algorithms (Table IV in Ivanova et al., 2014) shows that the open water tie points, about 205 K (37V) and 140 K (37H) are contained in the distributions for open water (dark blue curve in Figure 2(b) and (d)), the same is true for FYI: about 240 K (37V) and 230 K (37H), cf. the green curve in Figure 2(b) and (d). The MYI tie points however, about 190 K (37V) and 180 K (37H) however, are well above the mode of the corresponding distributions (red curves). The MYI tie points from the Antarctic “roundrobin data package” (see Table A1 in Ivanova et al., 2015) are even higher, 227 K (37V) and 205 K (37H) and thus at the very top end of our distributions. Interestingly, the considerably lower MYI tie points for Arctic MYI in both publications just mentioned are actually well contained in our (Antarctic) distributions. As to the C-band NRCS (Figure 2(a)), MYI has values between about -10dB and -5dB, while in the Arctic, values are usually lower, between about -15dB and -10dB (see, e.g., Lindell and Long, 2016).

For the correction schemes, we use lowest-level (2 m) air temperature data from meteorological reanalysis of the European Centre for Medium-Range Weather Forecast (ECMWF), namely, from the ERA Interim data set (Dee, 2011), the only source of comprehensive and consistent temperature data for the Antarctic sea ice areas (to be succeeded by ERA-5 data). We further use the low resolution sea ice drift product of the EUMETSAT Ocean and Sea Ice Satellite Application Facility (OSI SAF, [www.osi-saf.org](http://www.osi-saf.org), Lavergne et al., 2010). Note that sea ice motion data from the National Snow and Ice Data Center (NSIDC) (Tschudi et al., 2016, 2020) can also be used, and have actually already been used for the MYI retrieval in the Arctic (Ye et al., 2016b). At the time this study was started, the OSI-SAF drift data seemed the best choice, but the new NSIDC version 4 ice drift product might be an alternative. Sea ice drift data for the Antarctic are, however, less reliable than for the Arctic.

The used values of the tuning parameters for the temperature correction,  $N$ ,  $T_1$ ,  $T_2$ ,  $\Delta C_t$  (Section 2.2.1) are listed in Table 2, and the used values of the tuning parameters of the drift correction,  $\Delta C_d$ ,  $\Delta T_{19-37}$ , and  $T_{B,37H}$  (see Section 2.2.2) are listed in Table 3. For the time being, we have used the values that were used for the Arctic and fine-tuning might still improve the results, but for a “proof of concept” as which this study is intended this is sufficient. Besides, other issues might need attention first (see below, Section 3.2, “Discussion”).



**Figure 2.** Distribution of the four input parameters to ECICE for the Antarctic surface types of MYI (red), FYI (green), YI (cyan) and open water (blue): (a) ASCAT  $\sigma^0$  (top left); (b) AMSR2  $T_B$  at 37 GHz, V polarisation (top right); (c) AMSR2  $T_B$  at 37 GHz, H polarisation (bottom right); (d) and AMSR2  $GR(37V,19V)$  (bottom left).

**Table 2.** Tuning parameter setting for the **temperature correction** scheme

Parameter	Meaning	Value
$T_1$	thresh. temp., start of warm episode	-2°C
$T_2$	thresh. temp., end of warm episode	1°C
$N$	max. duration of warm episode	10 days
$\Delta C_t$	min. drop of MYI conc.	10%

The final result of the two-step retrieval method (i.e., ECICE and the corrections schemes) are MYI map data. In addition, as an intermediate result, a preliminary distinction of the sea ice into three types, i.e., MYI, FYI and YI (i.e., the “pure” ECICE output, without applying any correction) is produced as well. Hereinafter it is called “uncorrected YI, FYI, MYI concentration”.

**Table 3.** Tuning parameter setting for the **drift correction** scheme

Parameter	Meaning	Value
$\Delta C_d$	min. rise of MYI conc.	20%
$\Delta T_{37}$	min. drop of $T_{B,37H}$	20 K
$\Delta T_{19-37}$	min. drop of $T_{B,19H} - T_{B,37H}$	10 K

To date, we have retrieved data for the cold seasons 2013-2021. AMSR2 has been operational since August 2012, but since we need the start of the cold season for applying the drift correction, our retrieval starts with the year 2013. For each year, we have retrieved the ice type concentrations for the months of February to November (autumn, winter and spring). As the  
260 correction schemes need extra time to check for transient changes in MYI concentration and temporary warming events, the corrected MYI concentration is available from 22 February to 8 November each year (roughly the Antarctic freezing season) – see the example for YI, FYI and corrected MYI in Section 3.1.2 (Figure 4).

The AMSR-2 radiometer data as well as the ASCAT data are available within about 1 day of acquisition, thus, the uncorrected ice type concentrations can be retrieved in near real time with a time lag of one to two days. The corrected MYI concentration  
265 can be produced with an additional time lag of two weeks because of the corrections schemes, as just mentioned.

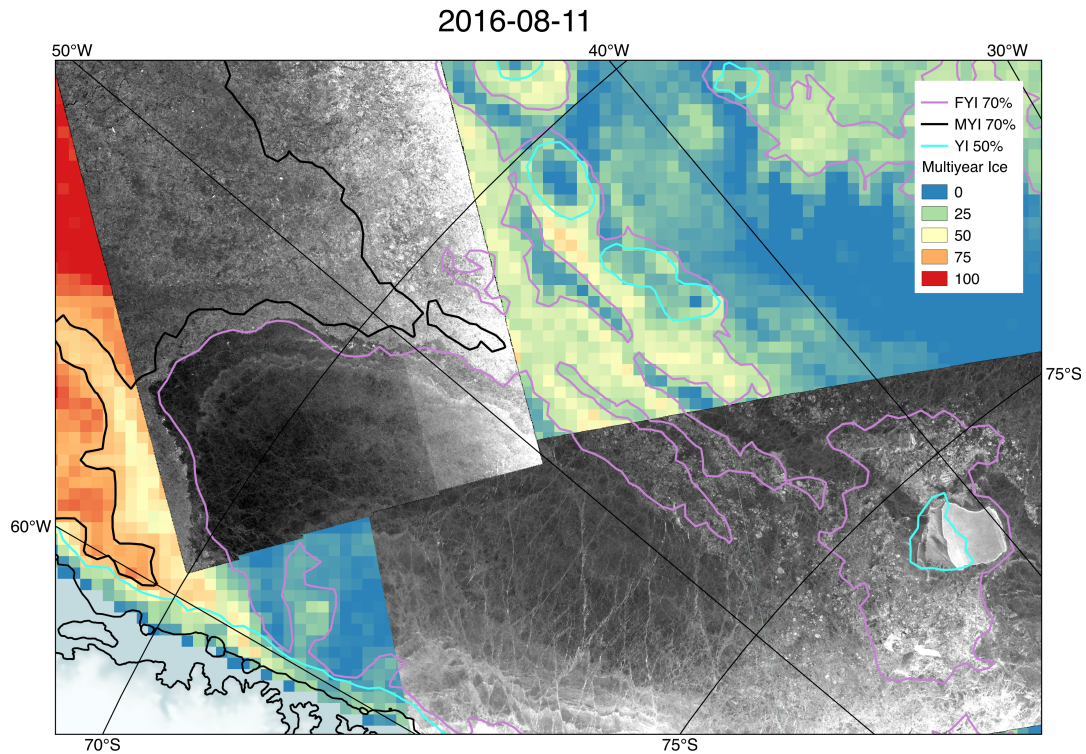
Note that retrieving Antarctic ice types in the freezing seasons of 2002-2011 is possible, using AMSR-E instead of AMSR2, and QuikSCAT instead of ASCAT before 2008. QuikSCAT uses a frequency of 13.4 GHz ( $K_u$  band) while ASCAT uses 5.4 GHz, so it is not trivial to switch. QuikSCAT, however, has already been used by us for the retrieval of Arctic MYI (see Ye et al., 2016a). For the years before 2013 (start of OSISAF drift data record for Antarctic), the sea ice drift data needed for  
270 the correction scheme of the MYI concentration are available from NSIDC (also used by Ye et al. (2016a)).

### 3 Results

#### 3.1 Comparison with other data

Validation of sea ice type concentration is a challenging task not only because there are few in-situ data sets of ice types available for the Antarctic region but also because point observations do not represent the large footprints of the satellite data.  
275 Validation studies using data from research cruises in the Antarctic have just started recently.

In this study we have compared the sea ice type concentration output from ECICE against three related satellite-based data sets: The new Antarctic uncorrected FYI and YI data and the corrected MYI data have been compared to data from (1) synthetic aperture radar (SAR) images, (2) charts showing the stage of development (SoD) of the ice, (3) maps of thin ice from the polynya data set mentioned above (but from a different year than those used for algorithm tuning). Examples are presented  
280 in the following.



**Figure 3.** Sentinel-1 SAR image (grey shade) acquired on 11 August, 2016, overlaid on MYI concentration (colour scale) of the same day from ECICE. Dominant ice type from ECICE indicated by contour lines. The legend shows only the most important colours for multiples of 25% concentration. The area is the inner (Southeastern) Weddell Sea, bordering the Antarctic Peninsula (lower left corner of the Figure).

### 3.1.1 Synthetic Aperture Radar (SAR) Images

As an initial “sanity check”, we have compared the MYI concentration from ECICE with high resolution SAR images acquired by Sentinel-1A/B at 40 m grid resolution (extra wide swath mode at HH polarisation). The focus was on the rather prominent FYI-MYI boundary in the Weddell Sea. In SAR images, MYI usually looks considerably brighter than FYI and YI because over time the surface has become more deformed (i.e., rougher) and the ice is more porous because of brine drainage so there is more volume scattering. For the comparison we manually scaled the radar backscatter to show good contrast between ice classes. We have examined 19 Sentinel-1 scenes from the two days 3 March and 11 August 2016 in the Weddell Sea and near the Antarctic Peninsula. Since the ECICE data represent a daily average (all AMSR and ASCAT swaths of one day are included), no correction for ice drift has been applied between the two data sets. An example is presented in Figure 3, showing an area in the Weddell Sea on 11 Aug, 2016. The Sentinel-1 SAR image (grey shade) is overlaid on the MYI concentration (colour scale). In addition, the dominant ice type is indicated by the coloured contours; white: YI=50%; purple: FYI=70%; black: MYI=70%.



The black and purple contours, which mark the transition from MYI to FYI, coincide well with a clear boundary between bright and dark radar backscatter which marks the boundary between dominating MYI and dominating FYI. Note also that  
295 ECICE correctly identifies an area of YI in the lee of the grounded iceberg A23A. The iceberg itself is retrieved as mixed type sea ice as it is outside the 70% of FYI or MYI and outside the 50% contour of YI. Qualitatively, the comparison to the other Sentinel-1 SAR scenes is similarly good.

### 3.1.2 Stage of Development (SoD) Charts

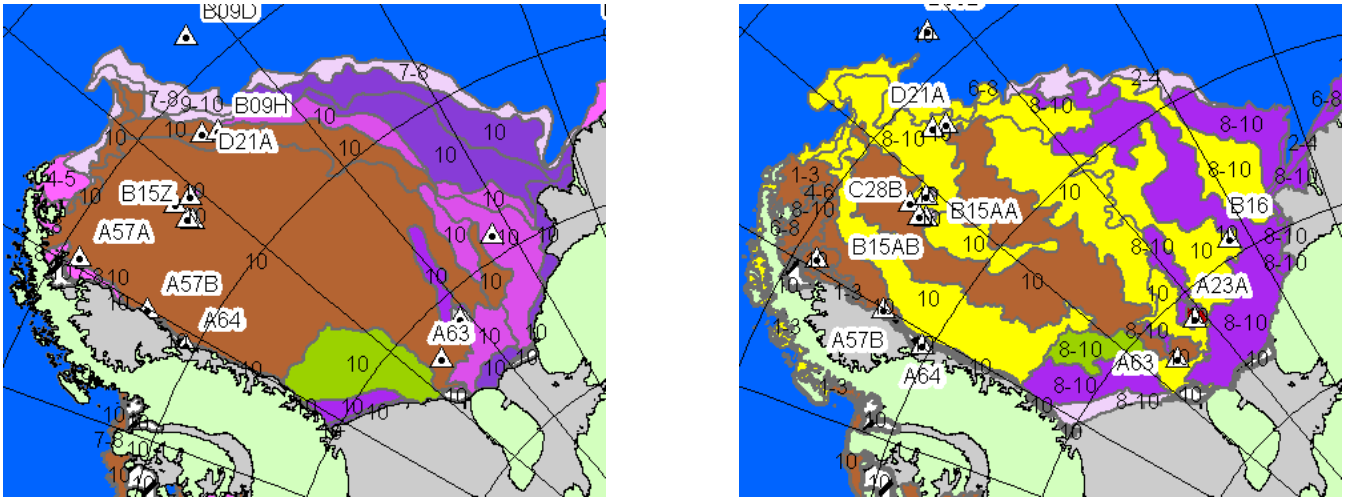
Weekly charts of the stage of development (SoD) of the Antarctic sea ice have been jointly produced by the U.S. National Ice  
300 Center (NIC) and the Russian Arctic and Antarctic Research Institute (AARI) since June 2015 (*AARI-NIC-NMI pilot project on integrated sea ice analysis for Antarctic waters*, <http://ice.aari.aq/antice/>). The charts, based on analysis of visible/infrared and microwave satellite imagery and reconnaissance data by experienced specialists, show various ice types, grouped roughly into YI, FYI, MYI. In this classification, the surface is divided into polygons each of which is assigned a single ice type. Purple tones indicate various types of YI, including nilas and grey ice (thickness up to 30 cm); yellow and green tones indicate  
305 various types of FYI (thickness above 30 cm); brown, orange and red indicate MYI. However, no distinction is made between *thick first-year ice* and *residual ice*, i.e. FYI that has survived the summer melt and has started a new cycle of growth. In the Antarctic, it is relabelled *second-year ice* only after July 1 (JCOMM Expert Team on Sea Ice, 2015; WMO, 2014).

We have compared the weekly SoD charts of the cold seasons (March to October) of 2017 and 2018 with our ice type data, and also done sporadic comparisons with data from other years. Some examples are presented below. There is an overall  
310 correspondence of the ice types from the charts and the dominant ice type in our data. An example is presented in Figure 4, showing (left to right, top to bottom) the Antarctic SoD chart from AARI (for the week that ends on 30 March, 2017), along with the YI and FYI concentrations from ECICE, and the corrected MYI concentration from ECICE plus correction schemes for 30 March, 2017. The SoD chart has been cropped to save space, the colour legend can be found in the Appendix B (Table B1). Note the YI (purple tones) in the Eastern Weddell Sea, in the Ross Sea and mainly along the Eastern Antarctic coast. The areas  
315 of MYI are in the Western Weddell Sea, in the Amundsen Sea and at the coast of Wilkes Land (130°–170°E).

At this early stage of the freezing season, the charts from AARI and from NIC often disagree on the MYI-FYI distinction. As an example Figure 5 shows the Weddell Sea on the same date of 30 March, 2017. The NIC chart (on the right) shows large strips of FYI (yellow) and MYI (“old ice”, brown), while the AARI chart (on the left) just shows MYI (and is much closer to the results of our retrieval, see previous figure). From April 2017 on, however, both the AARI and the NIC charts show a large  
320 and compact area of MYI in the Weddell Sea (so the strips of FYI marked in yellow in the NIC charts have been re-labelled MYI in brown).

A feature that is very well reproduced by the ice type maps in most years is the drifting of the MYI, adjacent to the Ronne Ice Shelf in the inner Weddell Sea at the beginning of the freezing season, towards the North and North-East in the subsequent months, shown for 2017 in Figure 6: The columns show charts and maps of the inner Weddell Sea for 16 March, 27 April, 25  
325 May, and 6 July, 2017; namely (top to bottom), SoD, corrected MYI, YI and FYI. The corrected MYI concentration (second row) has a sharp inner (Southern) boundary that agrees well with the boundary between MYI (brown) and YI (purple) or FYI



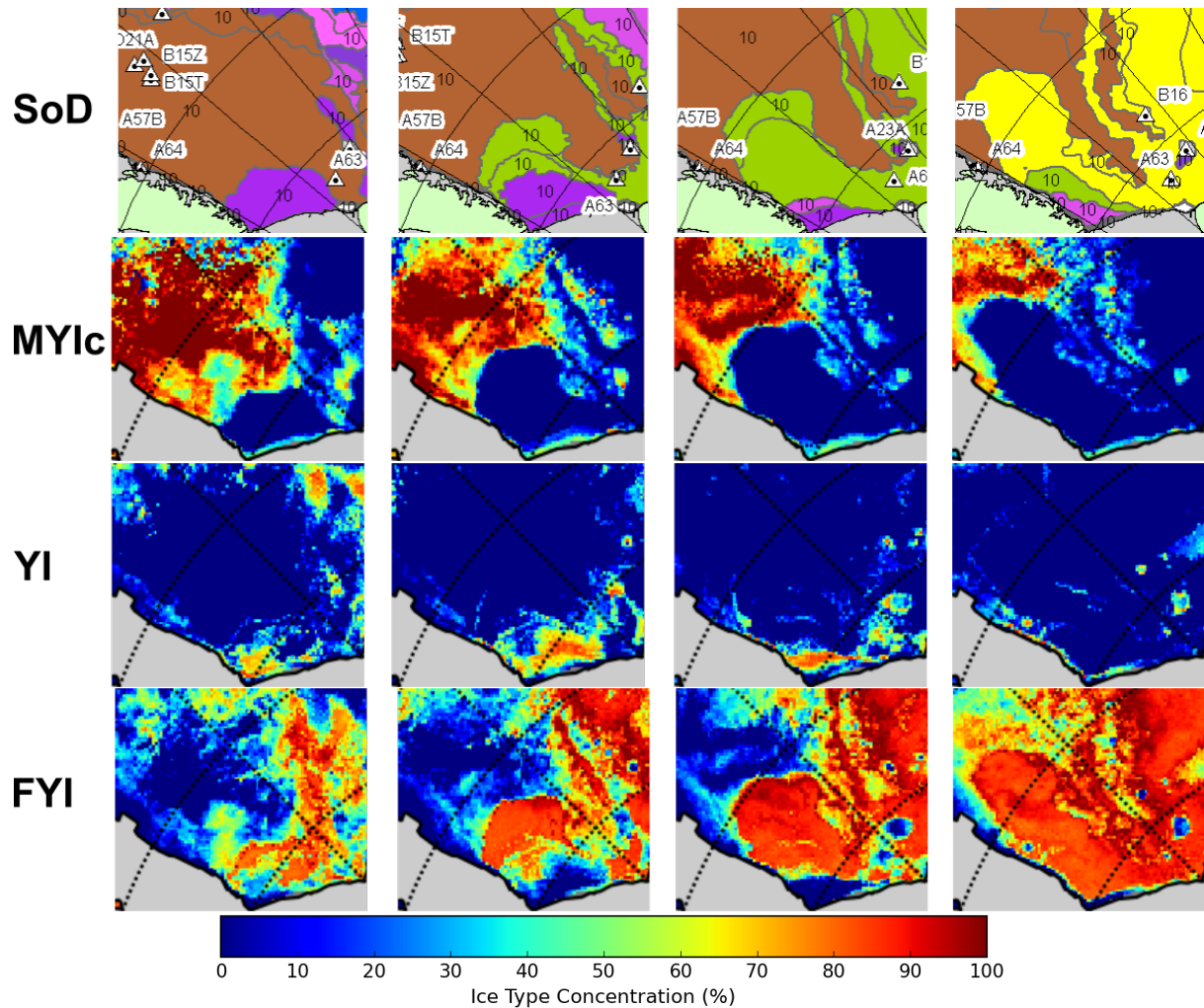


**Figure 5.** Stage of Development (SoD) charts of the Weddell Sea, 30 March, 2017, from AARI (left) and NIC (right). FYI is yellow, MYI (“old ice”) brown (see also colour legend in Appendix B, Table B1). The triangle symbols denote large icebergs.

(green and yellow) classes in the SoD charts (top row). The MYI and its inner boundary move towards North and North-East from March to July (left to right). Note the similarity to the FYI-MYI boundary in the previous Section 3.1.1 (Figure 3), and the two strips of MYI separated by FYI in the right part of the rightmost two SoD charts: The MYI strips correspond to similarly shaped areas with MYI concentration above about 30% to 40% in the MYIc maps (second row). The FYI areas in the SoD maps, in turn, correspond rather to FYI concentrations (fourth row) above about 60% to 70%. This hints at the difficulty of comparing a sea ice classification where each point is assigned exactly one sea ice type class with a sea ice type fraction retrieval where in each grid cell, more than one surface type can coexist with the summation of their fractions (including the open-water fraction) equal to 100%. The YI and FYI concentration in Figure 6 (third and fourth row) also match reasonably well with the SoD charts, noting that here as well, areas with YI concentration above about 30% correspond to the class YI in the SoD charts, and only FYI concentrations above about 70% correspond to the FYI classes in the SoD charts. This is best visible on the first two maps from the left. Another noteworthy detail are the small patches of YI apparently in the lee of grounded iceberg A23A (third and fourth column). The iceberg itself seems to be marked by almost zero FYI concentration (see the “holes” in the fourth row, FYI, last two panels).

### 3.1.3 Polynya Data Set PSSM

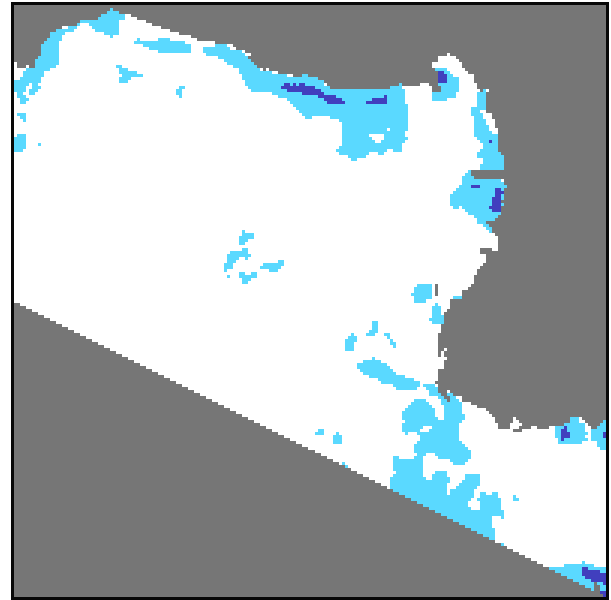
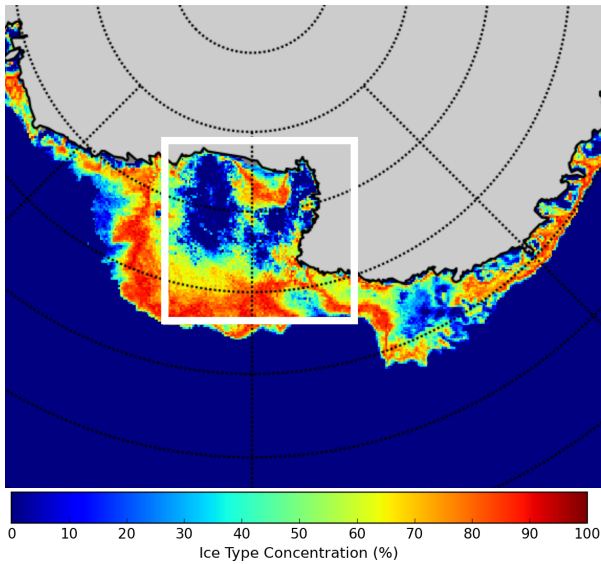
A further comparison was made with the already mentioned polynya data based on microwave brightness temperatures from SSMIS (see Section 2.3), from the year 2017, thus avoiding, of course, the data used for the probability distribution extraction which were from 2018 (Section 2.3). Figures 7 and 8 are examples of an area in the Ross Sea, near the Ross Ice Shelf, on 3 May and 7 September, 2018, respectively: the left panels of both figures show the map of YI concentration from ECICE; the right panels show PSSM maps with the surface type classes open water (dark blue), thin ice (light blue) and other ice (white).



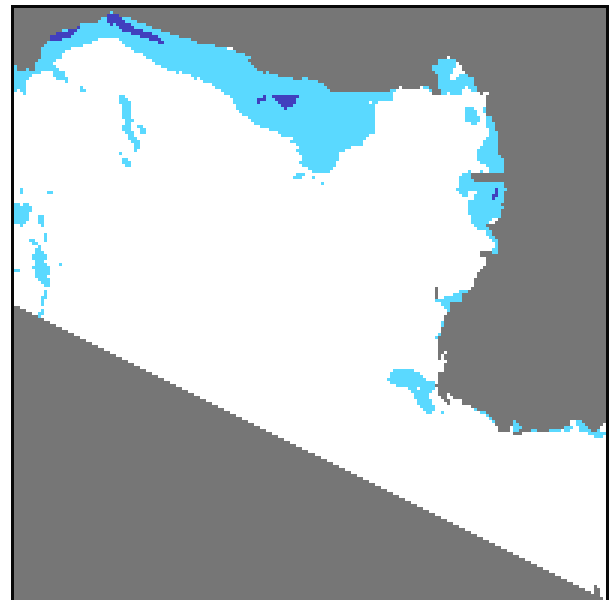
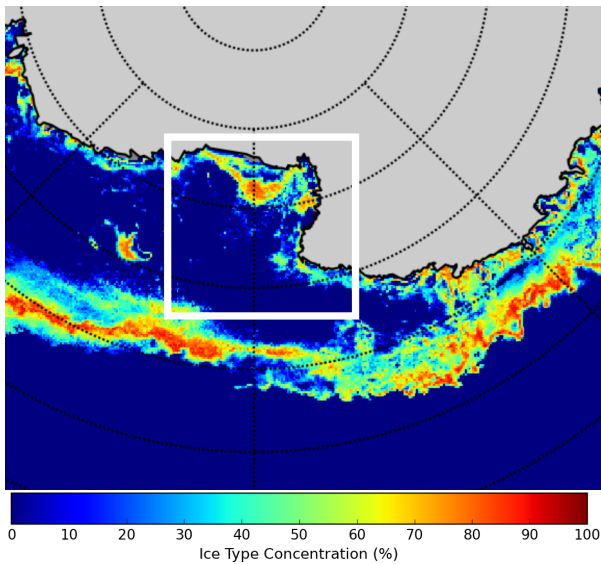
**Figure 6.** Southwestern Weddell Sea, March to July 2017, top to bottom: SoD chart from AARI, corrected MYI (MYIc), YI, FYI concentration; left to right: 16 March, 27 April, 25 May, 6 July, 2017.

Masked out areas (land, non-coastal sea) are shown in grey. The thin ice areas in the polynya data set match the dominantly YI areas from the ECICE retrieval.

Figures 9 and 10 show similar examples from the Weddell Sea, on 2 May, and 19 May, 2017, respectively, demonstrating the variability of coastal polynyas and the young ice associated with them: The thin ice (light blue) in the PSSM maps on the right corresponds roughly to YI concentrations above about 50% (green-yellow-orange) in the retrieved YI maps on the left. On 2 May (Figure 9), there is a large polynya covered with thin ice in the Southwestern Weddell Sea (light blue at the bottom centre of PSSM map on the right) and also coastal polynyas at the Brunt and the Riiser-Larsen Ice Shelves (top right of the PSSM map). Both are matched by high concentrations (orange hues) of YI in the map on the left. On May 19, however

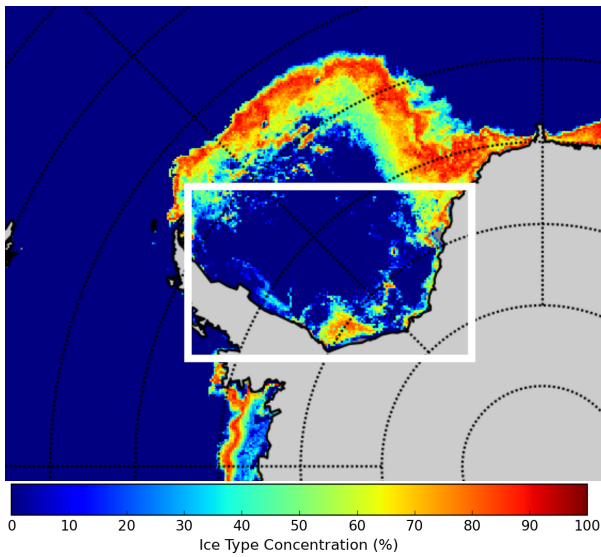


**Figure 7.** Left: map of YI, 3 May, 2017, right: PSSM polynya map in the area indicated by the white rectangle in the YI map (dark blue: open water, light blue: thin ice, white: other ice, grey: masked-out area).

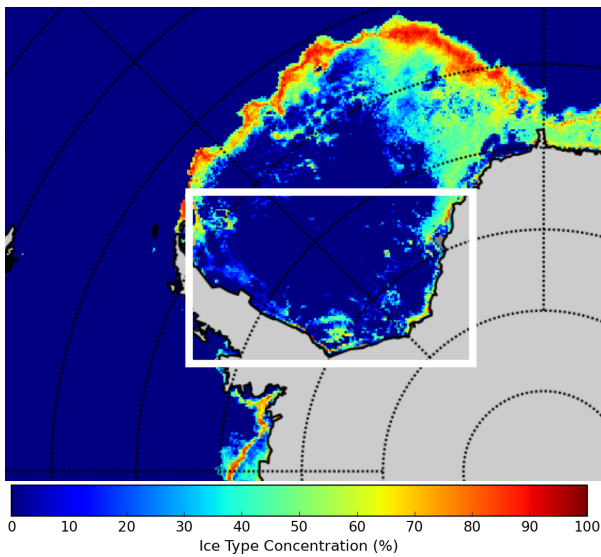


**Figure 8.** Left: map of YI, 7 Sep., 2017, right: PSSM polynya map in the area indicated by the white rectangle in the YI map (dark blue: open water, light blue: thin ice, white: other ice, grey: masked-out area).

(Figure 10), there is much less polynya activity according to the PSSM map, and also no areas of more than about 40% YI in  
 355 the map on the left.



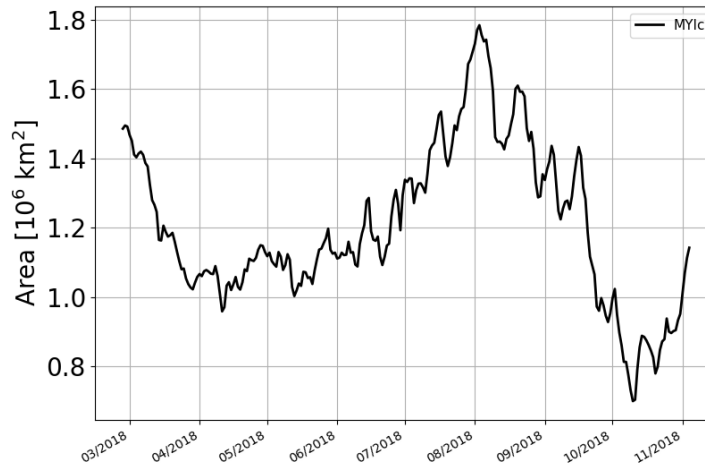
**Figure 9.** Left: map of YI, 2 May, 2017, right: PSSM polynya map in the area indicated by the white rectangle in the YI map (dark blue: open water, light blue: thin ice, white: other ice, grey: masked-out area).



**Figure 10.** Left: map of YI, 19 May, 2017, right: PSSM polynya map in the area indicated by the white rectangle in the YI map (dark blue: open water, light blue: thin ice, white: other ice, grey: masked-out area).

### 3.2 Discussion

As shown in the previous section, the retrieved corrected MYI (MYI<sub>c</sub>), and also the uncorrected FYI and YI concentrations, compare mostly well with other data, given the limitation that a rigorous validation could not be done yet.



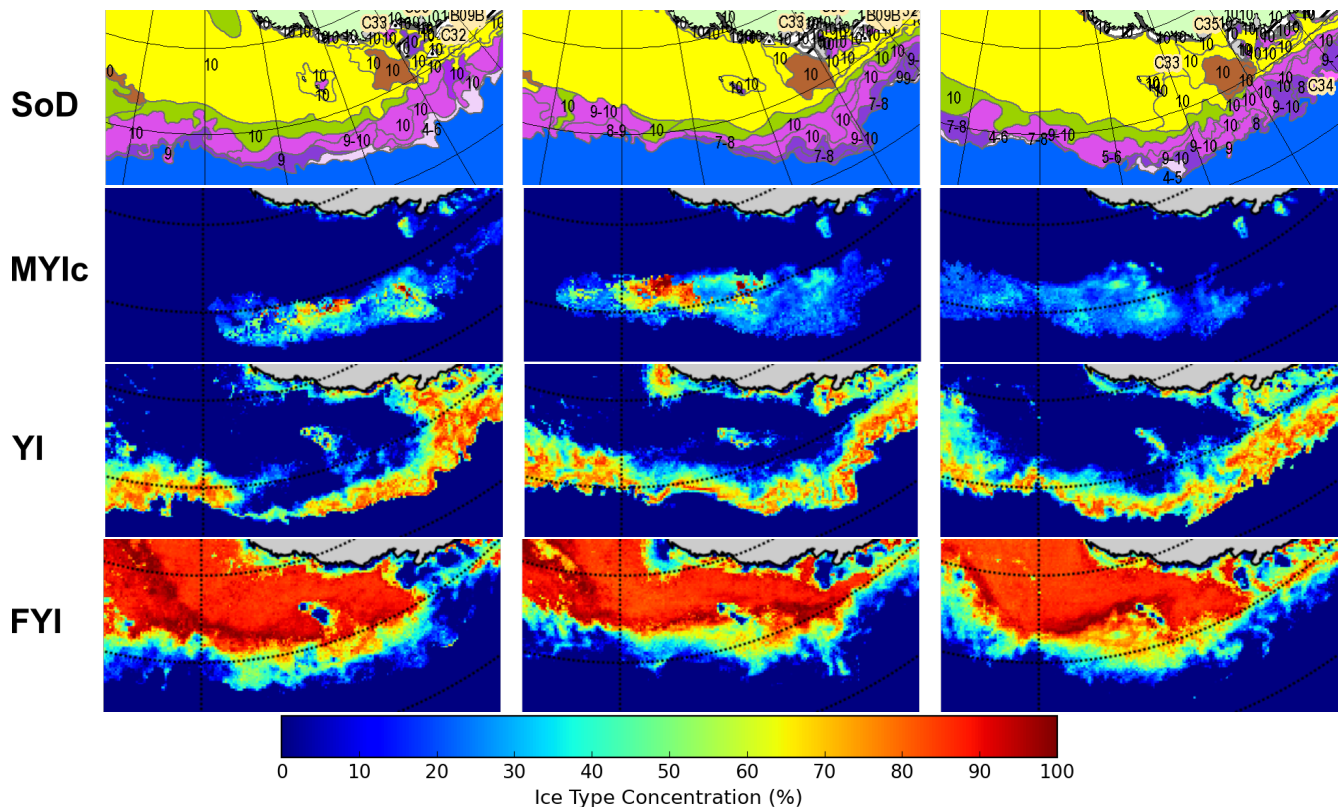
**Figure 11.** Time series of the total area of corrected MYI in the entire Antarctic, March to November 2018.

Large icebergs seem to be retrieved as MYI, but we have not looked further into that topic as the position and extent of such icebergs is usually well known and monitored, so they can be masked out using ancillary iceberg data (e.g., <https://usicecenter.gov/Products/AntarcticIcebergs>).

The total area of MYI in the entire Antarctic should not increase during one cold season because MYI originates as the remaining ice at the end of the melting season and hence cannot be generated after freeze-up. However, the total MYI area derived from our data shows large fluctuations, and in most years even an increase around July (see also Section 3.3). An example can be seen in Figure 11 which shows the total MYI area for all Antarctic seas for the cold season 2018. The total MYI area is calculated by multiplying the MYI concentration (0%–100%) of each grid cell with the area of the grid cell (taking into account that in a polar stereographic grid the grid cell area depends on the latitude).

The main reason for the increase in July seems to be a large offshore area of MYI in the outer Ross sea and off Wilkes Land, East of the Ross Sea (roughly between 160°E and 140°W, and between 65° and 70°S) that often seems to grow during the cold season and is not eliminated by the drift correction. Figure 12 shows such an area of MYI that appears in late July, 2018, and disappears in September. While, according to the NIC/AARI ice type (SoD) charts, a considerable area of MYI persists far offshore in the outer Ross Sea in many years (though not in the year 2018 shown here), the retrieved offshore MYI areas are larger, in different locations, and sometimes grow quickly within days, which cannot be correct and is not shown on the SoD charts. As MYI cannot be generated during the freezing season, this is clearly spurious identification of MYI. This area of spurious MYI is in the marginal ice zone. A similar phenomenon can be observed at around the same time in that region in all years of the current data record 2013 to 2021 though it is less pronounced in 2013 and 2017. The most likely reason for this is that in the course of the cold season, the snow layer on FYI in particular in the marginal ice zone changes. Usually, snow backscatter increases with time and emissivity decreases, making it resemble MYI in that respect (see also Willmes et al.,





**Figure 12.** Outer Ross Sea, off Wilkes Land, August and September , 2018, top to bottom: SoD chart from AARI, corrected MYI, YI, FYI concentration; left to right: 2 Aug, 30 Aug, 27 Sep, 2018.

2011; Arndt et al., 2016; Arndt and Haas, 2019). In addition, pancake ice has higher backscatter than FYI and might also be  
 380 mistaken for MYI. Elsewhere in the Antarctic seas, such areas of spurious MYI ice can also occur but are generally much  
 smaller. In principle, spurious MYI showing up during the cold season should be removed by the drift correction. The fact that  
 this fails can have two possible reasons: (1) problems in the ice drift data used by the drift correction, such as wrong direction  
 or wrong speed - a single drift vector that is much too large can initiate a growing area of spurious MYI (we also add one pixel  
 of uncertainty margin to the drift which might also cause the MYI domain to wrongly extend - cf. Section 2.2.2); (2) single  
 385 fixed points that permanently, but wrongly show MYI at the beginning of the freezing season: spurious MYI showing up within  
 one day's drift of such a wrong MYI point will then not be removed. On the next day, spurious MYI next to that point will  
 not be removed either. In this way, what started as one wrong MYI pixel ("seeding pixel", so to say) can grow into a large  
 region of wrong MYI within weeks. Such seeding pixels can be caused by "land contamination" of the satellite measurement  
 in footprints directly at the coast or near small islands that are not properly masked. Since removing coastal MYI pixels and  
 390 extending the land mask before applying the correction had no effect on the spurious MYI pixels, the latter reason can be  
 ruled out. Thus, the reason is most likely inaccuracies in the drift data which accumulate over the season (strange drift vectors



have been observed in particular in the Ross sea near the date line; Ted Maksym, Woods Hole Oceanographic Institution, priv. comm., 2020).

395 However, before putting effort into finding a flaw in the drift correction that does not properly remove spurious MYI, it makes more sense to prevent the misclassification that leads to retrieval of spurious MYI by ECICE in the first place. To do this, the distributions of MYI, FYI, and YI in the different channels should be investigated, specifically in the outer Ross Sea and off Wilkes Land. The fact that YI in the marginal ice zone often is pancake ice (see above) has not sufficiently been taken into account by our focusing just on YI in polynyas. If these parameter distributions for the ice types in the Ross Sea differ significantly from those currently used (see Section 2.3), they should be adapted.

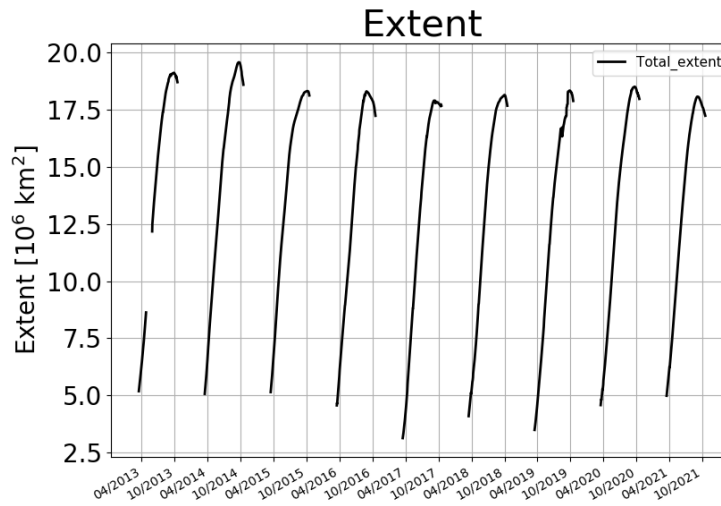
400 Towards the end of the freezing season, in September and October, the retrieved, corrected MYI concentration declines strongly in most years (see Figure 11), which is not seen in the weekly SoD charts. However, SoD charts seem to become unstable in the sense that the ice type oscillates between FYI (WMO type 2.5 “first-year ice” (JCOMM Expert Team on Sea Ice, 2015)) and MYI (WMO type 2.6 “old ice”) from one week to the next, or from AARI chart to the almost simultaneous NIC chart. The most likely reason for the too strong decline of MYI in our retrieval scheme are temperatures rising to near  
405 melting conditions which causes MYI to be misclassified as FYI as described above in Section 2.2.1 about the temperature correction. Since these near-melting or melting conditions are not episodic any more, they cannot be corrected by the temperature correction.

Note that a first analysis of the new OSI-SAF ice type classification data (Aaboe et al., 2021a) likewise does not show the expected decrease of Antarctic MYI area in the course of the season, but instead a steady slow increase followed by a rapid  
410 decline toward the end of the freezing season in September/October (Aaboe et al., 2021b, Fig. 14), which is similar to the time series derived from our data (Figure 11).

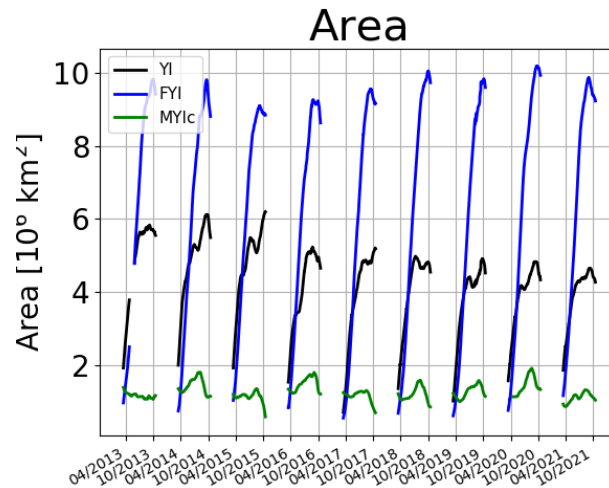
### 3.3 Time series 2013-2021

Having processed data from 2013 to 2021, we can now look at the longer time series. The problems with wrong MYI in the outer Ross Sea mainly start in the middle of the cold season, so, e.g., the MYI data in the beginning of the cold season should  
415 be more robust. Having nine consecutive seasons of ice type data, i.e., 2013–2021, we can have a look at how they evolve, in particular in view of the strong changes of the overall Antarctic sea ice extent since 2014: there was a record large sea ice extent in September 2014, then a record decline resulting in a record low in February 2017, and another record low in February 2022. A first check is to add up the concentration of the three ice types, which results in total sea ice, and compare the time series of its extent with the “standard” time series of sea ice extent based on data that do not distinguish between sea ice types, like the  
420 times series based on the ASI algorithm. Here (just for one plot) we use the common definition of extent as the total area of all grid cells with an ice concentration above 15%. Our time series shows the same ranking of the yearly maxima of Antarctic sea ice extent as the standard one, see Figure 13. As the sea ice type retrieval does not work well during melting season, the months November to February are masked out, so the yearly minima are not captured.

Now we can have a look at the total area of the three ice types – here we sum up the areas of all grid cells multiplied with  
425 their concentration (i.e., surface fraction) of the respective ice type. The result is shown in Figure 14. We see the steep rise of

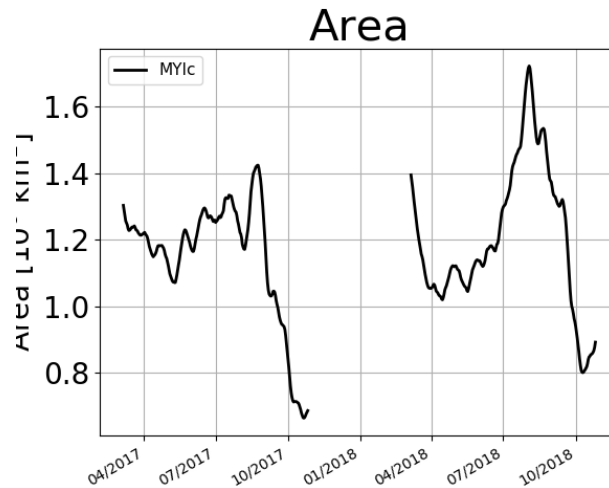


**Figure 13.** Total sea ice extent of the Antarctic sea ice, years 2013–2021, calculated from the sum of YI, FYI and MYI concentrations, smoothed with a 31-day moving average



**Figure 14.** Area of the three sea ice types YI (black), FYI (blue) and corrected MYI (green), years 2013–2021, March to October, smoothed with a 31-day moving average.

YI (black curve) and FYI (blue) at the beginning of each freezing season, the levelling off of the YI while the FYI continues to grow most of the season. The MYI area (green curve) in each season should not grow, which is not the case in most years: except for 2013 and 2017, there is a peak in the middle of the freezing season, which is, as mentioned in the previous section,



**Figure 15.** Area of corrected MYI, years 2017 and 2018, March to October, smoothed with a 11-day moving average.

mainly caused by erroneous MYI retrieval that is not adequately corrected by the corrections schemes, most notably in the  
 430 outer Ross Sea.

Figure 15 zooms in into just the corrected MYI area in 2017 and 2018 shows the extent of this erroneous rise that starts in July 2018 and amounts to about 50% of the area (from 1.2 million km<sup>2</sup> to 1.8 million km<sup>2</sup>)

The main question, however, is the interannual variability or change. In Figure 14, we see (1) a decline of the YI area maximum, (2) fluctuations of the FYI maximum that almost follow the maxima of total ice (Figure 13) – the extreme years  
 435 are not entirely the same; but (3) not much interannual change of the MYI area so far. Moreover, the MYI area seems hardly influenced by the strong fluctuations of total ice cover since 2014.

#### 4 Summary and Conclusions

The sea ice type retrieval method ECICE (Shokr et al., 2008; Shokr and Agnew, 2013) and the subsequent correction schemes for MYI (Ye et al., 2016a, b) developed for the Arctic can be adapted for the Antarctic, given samples of Antarctic ice types.  
 440 Input satellite data are microwave radiances at several channels as well as scatterometer backscattering measurements. Daily maps of uncorrected YI, FYI and MYI, and of MYI corrected for effects of melt-refreeze and snow metamorphosis, can be retrieved, during the freezing season, at grid resolution of 12.5 km. The results look reasonable in the sense that they show agreement with SAR images, with remote-sensing-based polynya data, and with weekly charted sea ice stage of development (so far the only source of detailed ice type information in the Antarctic, apart from ship-based observations of the ice con-  
 445 ditions). In particular, the general distribution of the Antarctic MYI at the beginning of the freezing season is well captured by our corrected ECICE results. The subsequent time evolution of the MYI concentration in the Weddell Sea, as far as the AARI/NIC stage of the development charts can tell, is captured as well in the months after freeze-up, showing the effects of

advection and melt. The retrieved distributions of YI and FYI concentration are reasonable as well. However, comparing our ice type concentrations, i.e., area fractions of ice types, with weekly charts that assign only one ice type to each location is inherently problematic. A more detailed validation study that also includes in-situ observations from research cruises is planned. The most problematic area is the outer Ross Sea and the sea off Wilkes Land, where large and growing areas of spurious MYI are retrieved in the marginal ice zone in late winter in most years. The data become unstable toward the end of the freezing season in September/October, with MYI probably being underestimated. The new time series, still preliminary, spanning the years 2013 to 2021, is the first comprehensive time series to give insight into the distribution and evolution of Antarctic sea ice types. A first look at it shows that the MYI area in the Antarctic has apparently not followed the strong fluctuations of the Antarctic total ice extent observed since 2014.

The current time series of uncorrected YI, FYI, MYI and MYIc can in principle be extended backwards to 2002, using AMSR-E and QuikSCAT data.

The next steps to establish a consolidated long-term time series of Antarctic MYI are, in order of importance: (1) derive new distributions for FYI and YI, possibly including pancake ice in FYI or YI; (2) use better ice drift data (e.g., NSIDC v.4); (3) use ERA-5 reanalysis data instead of ERA-Interim; (4) retrieve Antarctic MYI concentration for the years 2002–2011 (the “era” of AMSR-E); (5) comparison with in-situ and ship data where available.

Finally, the time series can be continued for the years to come, as the successor instrument of the radiometer AMSR2, namely, AMSR3, is scheduled for launch in 2023 or 2024 (see, e.g., Maeda et al., 2022), and scatterometers similar to ASCAT will be on the European MetOp Second Generation satellites B1, B2 and B3, from about 2025. In addition, there is the new Chinese-French Oceanography Satellite (CFO-Sat) carrying a  $K_u$  band scatterometer (Hauser et al., 2016), and the upcoming mission CIMR (Copernicus Imaging Microwave Radiometer, see Kilic et al., 2018) with radiometer channels from 1.4 to 36.5 GHz, that might even enable sea ice type retrieval without additional scatterometer data: At 1.4 GHz, the radiation emitted by sea ice at 1.4 GHz comes from a much thicker layer than emission at 19 GHz and higher. As MYI is less saline, has more air inclusions, thicker snow and is usually thicker than other ice types, MYI is likely to be distinct at 1.4 GHz.

*Data availability.* The uncorrected sea ice type data of the Antarctic, years 2013 to present, are available at the web site <http://seaice.uni-bremen.de>; the corrected MYI data of the Antarctic, years 2013–2019, are available on the same web site, and, in addition, as a data set in the PANGAEA archive, <https://doi.org/10.1594/PANGAEA.909054>

## Appendix A: Details on sample regions

ECICE needs the distribution of the input parameters,  $T_B(37V)$ ,  $T_B(37H)$ ,  $GR(37V, 19V)$ ,  $\sigma^\circ$  for the four different surface types, YI, MYI, FYI, open water. The Tables A1 and A2 list the geographical coordinates (latitude and longitude of lower left and upper right corner of rectangles in the NSIDC Antarctic maps used throughout in this paper), the dates on which the input parameters were sampled, and the number of samples (one sample is one grid point on one day). Table A1 lists the sampling


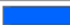
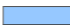
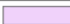















**Table A1.** Sample areas for YI in the Western Ross Sea. Note: lat. = latitude, lon. = longitude, no. = number

no.	lower left		upper right		date	no. of samples
	lat.	lon.	lat.	lon.		
1	71.91°S	179.09°W	73.56°S	175.6°E	28 Mar 2018	195
2	76.22°S	179.05°E	77.14°S	171.0°E	28 Mar 2018	160
3	70.59°S	176.62°E	72.6°S	172.06°E	03 Apr 2018	220
4	75.07°S	178.02°E	76.01°S	173.17°E	03 Apr 2018	90
5	76.73°S	179.26°E	77.43°S	172.65°E	12 May 2018	96
6	76.1°S	178.34°E	77.38°S	172.94°E	25 May 2018	120
7	76.67°S	179.51°W	77.39°S	171.61°E	03 Jun 2018	136
8	76.03°S	177.41°E	77.19°S	172.52°E	19 Jun 2018	96
9	74.87°S	175.87°E	77.24°S	170.41°E	22 Jun 2018	176
10	76.26°S	177.13°E	77.14°S	171.0°E	27 Jul 2018	120
11	76.07°S	176.22°E	77.38°S	171.1°E	28 Jul 2018	117
12	76.54°S	177.06°W	77.51°S	173.66°E	08 Sep 2018	162
13	76.24°S	175.93°W	77.62°S	176.54°E	11 Sep 2018	168
14	76.21°S	177.85°E	77.07°S	170.54°E	19 Sep 2018	126
15	76.56°S	179.02°W	77.06°S	171.83°E	29 Oct 2018	90
16	75.92°S	177.9°E	76.77°S	172.01°E	07 Nov 2018	96

**Table A2.** Sample areas for MYI, FYI and open water (OW). Note: lat. = latitude, lon. = longitude, no. = number

surface type	lower left		upper right		date range	no. of samples
	lat.	lon.	lat.	lon.		
MYI	70.66°S	99.18°W	71.66°S	97.17°W	3 Mar – 4 Mar 2018	112
MYI	70.66°S	99.18°W	71.66°S	97.17°W	8 Mar – 9 Mar 2018	112
MYI	66.14°S	59.15°W	66.5°S	54.46°W	28 Feb – 4-Mar 2018	740
FYI	73.94°S	43.84°W	73.14°S	31.1°W	27 Apr – 30 Apr 2018	2100
FYI	69.31°S	23.24°W	67.47°S	14.95°W	11 Jun – 13 Jun 2018	1512
FYI	71.73°S	152.79°W	75.46°S	158.7°W	21-Aug – 25-Aug 2018	3240
OW	51.15°S	130.48°W	58.56°S	129.33°W	21 Aug – 25 Aug 2018	12500
OW	74.28°S	172.87°W	76.43°S	177.09°E	1 Mar – 3 Mar, 2018	1242

areas for YI (from the polynyas in the Western Ross Sea), and Table A2 lists the sampling areas for MYI, FYI and open water (OW).

Colour		RGB colour model	Stage of development (SoD)	Number from WMO Sea Ice Nomenclature
alternative	prime			
		000-100-255	Ice free	4.2.8
		150-200-255	<1/10 ice of unspecified SoD (open water)	4.2.6
		240-210-250	New ice	2.1
		255-175-255	Dark nilas	2.2.1
		255-100-255	Light nilas	2.2.2
		170-040-240	Young ice	2.4
		135-060-215	Grey ice	2.4.1
		220-080-235	Grey-white ice	2.4.2
		255-255-000	First-year ice (FY)	2.5
		155-210-000	FY thin ice (white ice)	2.5.1
		215-250-130	FY thin ice (white ice) first stage	2.5.1.1
		175-250-000	FY thin ice (white ice) second stage	2.5.1.2
		000-200-020	FY medium ice	2.5.2
		000-120-000	FY thick ice	2.5.3
		180-100-050	Old ice	2.6
		000-120-000	Residual ice	2.6.1
		255-120-010	Second-year ice	2.6.2
		200-000-000	Multi-year ice	2.6.3

**Table B1.** Colour coding of the sea ice types in the ice charts shown above

## Appendix B: WMO colour coding of sea ice types

The AARI/NIC ice charts showing the stage of development in Figures 4 to 12 use the colour code specified by WMO (2014). For easier reference, the colour codes of the ice types relevant here are shown in Table B1.

*Author contributions.* CM has adapted the algorithm and correction schemes for the Antarctic, has written the initial manuscript and revised it; YY has developed the original correction schemes for the Arctic and has given feedback and advice for the work; MS has contributed the original ECICE retrieval which is the basis of the whole retrieval, has given important feedback and advice and contributed substantially to the revision; GS has contributed the comparison with SAR data, and has given critical scientific advice in all stages of the work; all co-authors have reviewed the manuscript.

*Competing interests.* The authors declare that they have no competing interests.

*Acknowledgements.* This work was supported by the Deutsche Forschungsgemeinschaft (DFG), project SITAnt, grant SP1128/2-1, in the framework of the Antarctic priority programme SPP 1158 “Antarctic Research with comparative investigations in Arctic ice areas”. The authors acknowledge the International Space Science Institute (ISSI) in Bern for support and for discussions in the ISSI team “Satellite-Derived

Estimates of Antarctic Snow and Ice Thickness” led by P. Heil, University of Tasmania. The authors are very grateful to S. Kern, University of Hamburg, for producing and providing the polynya data set, and to S. Arndt and C. Haas, Alfred Wegener Institute, Bremerhaven, for  
495 important discussions.

## References

- Aaboe, S., Down, E. J., and Eastwood, S.: Algorithm Theoretical Basis Document for the Global Sea-Ice Edge and Type Product, Version 3.3, Tech. rep., EUMETSAT Ocean and Sea Ice SAF, [https://osisaf-hl.met.no/sites/osisaf-hl.met.no/files/baseline\\_document/osisaf\\_cdop3\\_ss2\\_atbd\\_sea-ice-edge-type\\_v3p3.pdf](https://osisaf-hl.met.no/sites/osisaf-hl.met.no/files/baseline_document/osisaf_cdop3_ss2_atbd_sea-ice-edge-type_v3p3.pdf), 2021a.
- 500 Aaboe, S., Down, E. J., and Eastwood, S.: Validation Report for the Global Sea-Ice Edge and Type Product, Version 3.1, Tech. rep., EUMETSAT Ocean and Sea Ice SAF, [https://osisaf-hl.met.no/sites/osisaf-hl.met.no/files/validation\\_reports/osisaf\\_cdop3\\_ss2\\_svr\\_sea-ice-edge-type\\_v3p1.pdf](https://osisaf-hl.met.no/sites/osisaf-hl.met.no/files/validation_reports/osisaf_cdop3_ss2_svr_sea-ice-edge-type_v3p1.pdf), 2021b.
- Arndt, S. and Haas, C.: Spatiotemporal variability and decadal trends of snowmelt processes on Antarctic sea ice observed by satellite scatterometers, *The Cryosph.*, 13, 1943–1958, <https://doi.org/10.5194/tc-13-1943-2019>, 2019.
- 505 Arndt, S., Willmes, S., Dierking, W., and Nicolaus, M.: Timing and regional patterns of snowmelt on Antarctic sea ice from passive microwave satellite observations, *J. Geophys. Res. Oceans*, 121, 5916–5930, <https://doi.org/10.1002/2015JC011504>, 2016.
- Comiso, J. C.: Large Decadal Decline of the Arctic Multiyear Ice Cover, *Journal of Climate*, 25, 1176–1193, <https://doi.org/10.1175/jcli-d-11-00113.1>, 2012.
- Dee, D. P.: The ERA-Interim reanalysis: Configuration and performance of the data assimilation system, *Q. J. Roy. Meteor. Soc.*, 137, 553–597, <https://doi.org/10.1002/qj.828>, 2011.
- 510 Drobot, S. D. and Anderson, M. R.: An improved method for determining snowmelt onset dates over Arctic sea ice using scanning multichannel microwave radiometer and Special Sensor Microwave/Imager data, *J. Geophys. Res.*, 106, 24033–24049, <https://doi.org/10.1029/2000JD000171>, 2001.
- Gow, A., Ackley, S., Buck, K., and Golden, K.: 1987 Physical and structural characteristics of Weddell Sea pack ice, *Crrel rep.* 87–14., Cold Regions Research and Engineering Laboratory (CREL), 1987.
- Haas, C., Thomas, D. N., and Bareiss, J.: Surface properties and processes of perennial Antarctic sea ice in summer, *Journal of Glaciology*, 47, 613–625, <https://doi.org/10.3189/172756501781831864>, 2001.
- Hauser, D., Xiaolong, D., Aouf, L., Tison, C., and Castillan, P.: Overview of the CFOSAT mission, in: 2016 IEEE International Geoscience and Remote Sensing Symposium (IGARSS), pp. 5789–5792, <https://doi.org/10.1109/IGARSS.2016.7730512>, 2016.
- 520 Hobbs, W. R., Bindoff, N. L., and Raphael, M. N.: New Perspectives on Observed and Simulated Antarctic Sea Ice Extent Trends Using Optimal Fingerprinting Techniques, *J. Clim.*, 28, 1543–1560, <https://doi.org/10.1175/JCLI-D-14-00367.1>, 2015.
- Ivanova, N., Johannessen, O. M., Pedersen, L. T., and Tonboe, R. T.: Retrieval of Arctic Sea Ice Parameters by Satellite Passive Microwave Sensors: A Comparison between Eleven Sea Ice Concentration Algorithms, *IEEE T. Geosci. Remote*, 52, 7233–7246, <https://doi.org/10.1109/TGRS.2014.2310136>, 2014.
- 525 Ivanova, N., Pedersen, L. T., Tonboe, R. T., Kern, S., Heygster, G., Lavergne, T., Sørensen, A., Saldo, R., Dybkjær, G., Brucker, L., and Shokr, M.: Inter-comparison and evaluation of sea ice algorithms: towards further identification of challenges and optimal approach using passive microwave observations, *The Cryosph.*, 9, 1797–1817, <https://doi.org/10.5194/tc-9-1797-2015>, 2015.
- JCOMM Expert Team on Sea Ice: WMO Sea Ice Nomenclature, volumes I, II, and II (WMO-259), Tech. rep., World Meteorological Organization, [https://library.wmo.int/doc\\_num.php?explnum\\_id=4651](https://library.wmo.int/doc_num.php?explnum_id=4651), 2015.
- 530 Johannessen, O. M., Shalina, E. V., and Miles, M. W.: Satellite Evidence for an Arctic Sea Ice Cover in Transformation, *Science*, 286, 1937–1939, <https://doi.org/10.1126/science.286.5446.1937>, 1999.



- Kern, S., Spreen, G., Kaleschke, L., De La Rosa, S., and Heygster, G.: Polynya Signature Simulation Method polynya area in comparison to AMSR-E 89GHz sea-ice concentrations in the Ross Sea and off the Adélie Coast, Antarctica, for 2002: first results, *Ann. Glaciol.*, 46, 409–418, <https://doi.org/10.3189/172756407782871585>, 2007.
- 535 Kilic, L., Prigent, C., Aires, F., Boutin, J., Heygster, G., Tonboe, R. T., Roquet, H., Jimenez, C., and Donlon, C.: Expected Performances of the Copernicus Imaging Microwave Radiometer (CIMR) for an All-Weather and High Spatial Resolution Estimation of Ocean and Sea Ice Parameters, *J. Geophys. Res. Oceans*, 123, 7564–7580, <https://doi.org/10.1029/2018JC014408>, 2018.
- Kwok, R.: Arctic sea ice thickness, volume, and multiyear ice coverage: losses and coupled variability (1958–2018), *Env. Res. Lett.*, 13, 105 005, <https://doi.org/10.1088/1748-9326/aae3ec>, 2018.
- 540 Lange, M., Ackley, S., Wadhams, P., Dieckmann, G., and Eicken, H.: Development of Sea Ice in the Weddell Sea, *Annals of Glaciology*, 12, 92–96, <https://doi.org/10.3189/S0260305500007023>, 1989.
- Lange, M. A. and Eicken, H.: Textural characteristics of sea ice and the major mechanisms of ice growth in the Weddell Sea, *Annals of Glaciology*, 15, 210–215, <https://doi.org/10.3189/1991AoG15-1-210-215>, 1991.
- Lavergne, T., Eastwood, S., Teffah, Z., Schyberg, H., and Breivik, L.-A.: Sea ice motion from low resolution satellite sensors: an alternative  
545 method and its validation in the Arctic, *J. Geophys. Res.*, 115, C10032, <https://doi.org/10.1029/2009JC005958>, 2010.
- Lindell, D. B. and Long, D. G.: Multiyear Arctic Ice Classification Using ASCAT and SSMIS, *Remote Sensing*, 8, <https://doi.org/10.3390/rs8040294>, 2016.
- Ludescher, J., Yuan, N., and Bunde, A.: Detecting the statistical significance of the trends in the Antarctic sea ice extent: an indication for a turning point, *Climate Dynamics*, 53, 237–244, <https://doi.org/10.1007/s00382-018-4579-3>, 2019.
- 550 Lythe, M., Hauser, A., and Wendler, G.: Classification of sea ice types in the Ross Sea, Antarctica from SAR and AVHRR imagery, *Int. J. Remote Sens.*, 20, 3073–3085, <https://doi.org/10.1080/014311699211624>, 1999.
- Maeda, T., Tomii, N., Seki, M., Sekiya, K., Taniguchi, Y., and Shibata, A.: Validation of Hi-Resolution Sea Surface Temperature Algorithm Toward the Satellite-Borne Microwave Radiometer AMSR3 Mission, *IEEE Geoscience and Remote Sensing Letters*, 19, 1–5, <https://doi.org/10.1109/LGRS.2021.3066534>, 2022.
- 555 Mahlstein, I., Gent, P. R., and Solomon, S.: Historical Antarctic mean sea ice area, sea ice trends, and winds in CMIP5 simulations, *J. Geophys. Res.*, 118, 5105–5110, <https://doi.org/10.1002/jgrd.50443>, 2013.
- Markus, T. and Burns, B. A.: A method to estimate subpixel-scale coastal polynyas with satellite passive microwave data, *J. Geophys. Res. Oceans*, 100, 4473–4487, <https://doi.org/10.1029/94JC02278>, 1995.
- Massom, R., Giles, A., Fricker, H., Legresy, B., Warner, R., Hyland, G., Young, N., and Fraser, A.: Examining the interaction between multi-  
560 year landfast sea ice and the Mertz Glacier Tongue, East Antarctica: Another factor in ice sheet stability?, *J. Geophys. Res. Oceans*, 115, C12027, <https://doi.org/10.1029/2009JC006083>, 2010.
- Melsheimer, C. and Spreen, G.: IUP Multiyear Ice Concentration and other sea ice types, Version 1.1 (Arctic)/Version AQ2 (Antarctic) – User Guide, Tech. rep., Institute of Environmental Physics, University of Bremen, <https://seaice.uni-bremen.de/data/MultiYearIce/MyIuserguide.pdf>, accessed: 2020-04-07, 2019.
- 565 Melsheimer, C. and Spreen, G.: AMSR2 ASI sea ice concentration data, Antarctic, version 5.4 (NetCDF) (July 2012 - December 2019), <https://doi.org/10.1594/PANGAEA.898400>, 2019.
- Meredith, M., Sommerkorn, M., Cassotta, S., Derksen, C., Ekaykin, A., Hollowed, A., Kofinas, G., Mackintosh, A., Melbourne-Thomas, J., Muelbert, M., Ottersen, G., Pritchard, H., and Schuur, E.: Polar Regions, in: IPCC Special Report on the Ocean and Cryosphere in a Changing Climate, edited by Pörtner, H.-O., Roberts, D., Masson-Delmotte, V., Zhai, P., Tignor, M., Poloczanska, E., Mintenbeck,

- 570 K., Alegría, A., Nicolai, M., Okem, A., Petzold, J., Rama, B., and Weyer, N., IPCC, <https://www.ipcc.ch/srocc/chapter/chapter-3-2/>, in press, 2019.
- Nihashi, S. and Ohshima, K. I.: Circumpolar Mapping of Antarctic Coastal Polynyas and Landfast Sea Ice: Relationship and Variability, *J. Clim.*, 28, 3650–3670, <https://doi.org/10.1175/JCLI-D-14-00369.1>, 2015.
- Ozsoy-Cicek, B., Kern, S., Ackley, S. F., Xie, H., and Tekeli, A. E.: Intercomparisons of Antarctic sea ice types from visual ship, RADARSAT-  
575 1 SAR, Envisat ASAR, QuikSCAT, and AMSR-E satellite observations in the Bellingshausen Sea, *Deep Sea Research Part II: Topical Studies in Oceanography*, 58, 1092–1111, <https://doi.org/10.1016/j.dsr2.2010.10.031>, 2011.
- Parkinson, C. L.: A 40-y record reveals gradual Antarctic sea ice increases followed by decreases at rates far exceeding the rates seen in the Arctic, *Proc. Natl. Acad. Sci. USA*, 116, 14 414–14 423, <https://doi.org/10.1073/pnas.1906556116>, 2019.
- Parkinson, C. L. and Cavalieri, D. J.: Antarctic sea ice variability and trends, 1979–2010, *The Cryosphere*, 6, 871–880,  
580 <https://doi.org/10.5194/tc-6-871-2012>, 2012a.
- Parkinson, C. L. and Cavalieri, D. J.: Arctic sea ice variability and trends, 1979–2010, *The Cryosphere*, 6, 881–889, <https://doi.org/10.5194/tc-6-881-2012>, 2012b.
- Parkinson, C. L. and DiGirolamo, N. E.: Sea ice extents continue to set new records: Arctic, Antarctic, and global results, *Remote Sens. Environ.*, 267, <https://doi.org/10.1016/j.rse.2021.112753>, 2021.
- 585 Polvani, L. M. and Smith, K. L.: Can natural variability explain observed Antarctic sea ice trends? New modeling evidence from CMIP5, *Geophys. Res. Lett.*, 40, 3195–3199, <https://doi.org/10.1002/grl.50578>, 2013.
- Shokr, M. and Agnew, T. A.: Validation and potential applications of Environment Canada Ice Concentration Extractor (ECICE) algorithm to Arctic ice by combining AMSR-E and QuikSCAT observations, *Remote Sens. Environ.*, 128, 315–332, <https://doi.org/10.1016/j.rse.2012.10.016>, 2013.
- 590 Shokr, M., Lambe, A., and Agnew, T.: A New Algorithm (ECICE) to Estimate Ice Concentration From Remote Sensing Observations: An Application to 85-GHz Passive Microwave Data, *IEEE Trans. Geosci. Remote Sens.*, 46, 4104–4121, <https://doi.org/10.1109/tgrs.2008.2000624>, 2008.
- Spreen, G., Kaleschke, L., and Heygster, G.: Sea Ice Remote Sensing Using AMSR-E 89 GHz Channels, *J. Geophys. Res.*, 113, C02S03, <https://doi.org/10.1029/2005JC003384>, 2008.
- 595 Stocker, T., Qin, D., Plattner, G.-K., Tignor, M., Allen, S., Boschung, J., Nauels, A., Xia, Y., Bex, V., and Midgley, P., eds.: *Climate Change 2013: The Physical Science Basis. Contribution of Working Group I to the Fifth Assessment Report of the Intergovernmental Panel on Climate Change*, Cambridge University Press, Cambridge, United Kingdom and New York, NY, USA, <https://doi.org/10.1017/CBO9781107415324>, 2013.
- Tschudi, M., Fowler, C., Maslanik, J., Stewart, J. S., and Meier, W.: Polar Pathfinder Daily 25 km EASE-Grid Sea Ice Motion Vectors, Version 3. (Arctic, Antarctic), NASA National Snow and Ice Data Center Distributed Active Archive Center. Boulder, Colorado USA,  
600 <https://nsidc.org/data/nsidc-0116/versions/3>, doi: 10.5067/O57VAIT2AYYY, 2016.
- Tschudi, M. A., Meier, W. N., and Stewart, J. S.: An enhancement to sea ice motion and age products at the National Snow and Ice Data Center (NSIDC), *The Cryosph.*, 14, 1519–1536, <https://doi.org/10.5194/tc-14-1519-2020>, 2020.
- Turner, J., Hosking, J. S., Bracegirdle, T. J., Marshall, G. J., and Phillips, T.: Recent changes in Antarctic Sea Ice, *Phil. Trans. R. Soc. A*,  
605 373, 20140163, <https://doi.org/10.1098/rsta.2014.0163>, 2015.
- Wadhams, P., Squire, V. A., Ewing, J. A., and Pascal, R. W.: The Effect of the Marginal Ice Zone on the Directional Wave Spectrum of the Ocean, *J. Phys. Oceanogr.*, 16, 358–376, [https://doi.org/10.1175/1520-0485\(1986\)016<0358:TEOTMI>2.0.CO;2](https://doi.org/10.1175/1520-0485(1986)016<0358:TEOTMI>2.0.CO;2), 1986.

- Wessel, P., Smith, W. H. F., Scharroo, R., Luis, J., and Wobbe, F.: Generic Mapping Tools: Improved Version Released, *Eos, Transactions AGU*, 94, 409–410, <https://doi.org/10.1002/2013EO450001>, 2013.
- 610 Willmes, S., Haas, C., and Nicolaus, M.: High radar-backscatter regions on Antarctic sea-ice and their relation to sea-ice and snow properties and meteorological conditions, *Int. J. Remote Sens.*, 32, 3967–3984, <https://doi.org/10.1080/01431161003801344>, 2011.
- WMO: Ice Chart Colour Code Standard, May 2014 edition (revision 1), Tech. rep., World Meteorological Organization, <https://jcomm.info/document/18296>, 2014.
- Ye, Y., Heygster, G., and Shokr, M.: Improving Multiyear Ice Concentration Estimates With Reanalysis Air Temperatures, *IEEE Trans. Geosci. Remote Sens.*, 54, 2602–2614, <https://doi.org/10.1109/tgrs.2015.2503884>, 2016a.
- 615 Ye, Y., Shokr, M., Heygster, G., and Spreen, G.: Improving Multiyear Sea Ice Concentration Estimates with Sea Ice Drift, *Remote Sensing*, 8, 397, <https://doi.org/10.3390/rs8050397>, 2016b.
- Ye, Y., Shokr, M., Aaboe, S., Aldenhoff, W., Eriksson, E. B. L., Heygster, G., Melsheimer, C., and Girard-Arduin, F.: Inter-comparison and evaluation of sea ice type concentration algorithms, *The Cryosph. Disc.*, <https://doi.org/10.5194/tc-2019-200>, 2019.
- 620 Zunz, V., Goosse, H., and Massonnet, F.: How does internal variability influence the ability of CMIP5 models to reproduce the recent trend in Southern Ocean sea ice extent?, *The Cryosph.*, 7, 451–468, <https://doi.org/10.5194/tc-7-451-2013>, 2013.